The oxidation state of Fe in MORB glasses and the oxygen fugacity of the upper mantle

Elizabeth Cottrell [a,*], Katherine A. Kelley [b]

[a] Department of Mineral Sciences, National Museum of Natural History, Smithsonian Institution, 10th & Constitution Ave., Washington DC, 20560, USA
[b] Graduate School of Oceanography, University of Rhode Island, Narragansett Bay Campus, Narragansett, RI 02882, USA

ABSTRACT

Micro-analytical determination of $Fe^{3+}/\sum Fe$ ratios in mid-ocean ridge basalt (MORB) glasses using micro X-ray absorption near edge structure (μ-XANES) spectroscopy reveals a substantially more oxidized upper mantle than determined by previous studies. Here, we show that global MORBs yield average $Fe^{3+}/\sum Fe$ ratios of 0.16 ± 0.01 (n = 103), which trace back to primary MORB melts equilibrated at the conditions of the quartz–fayalite–magnetite (QFM) buffer. Our results necessitate an upward revision of the $Fe^{3+}/\sum Fe$ ratios of MORBs, mantle oxygen fugacity, and the ferric iron content of the mantle relative to previous wet chemical determinations. We show that only 0.01 (absolute, or <10%) of the difference between $Fe^{3+}/\sum Fe$ ratios determined by micro-colorimety and XANES can be attributed to the Mössbauer-based XANES calibration. The difference must instead derive from a bias between micro-colorimetry performed on experimental vs. natural basalts. Co-variations of $Fe^{3+}/\sum Fe$ ratios in global MORB with indices of low-pressure fractional crystallization are consistent with Fe^{3+} behaving incompatibly in shallow MORB magma chambers. MORB $Fe^{3+}/\sum Fe$ ratios do not, however, vary with indices of the extent of mantle melting (e.g., $Na_2O(8)$) or water concentration. We offer two hypotheses to explain these observations: The bulk partition coefficient of Fe^{3+} may be higher during peridotite melting than previously thought, and may vary with temperature, or redox exchange between sulfide and sulfate species could buffer mantle melting at ~QFM. Both explanations, in combination with the measured MORB $Fe^{3+}/\sum Fe$ ratios, point to a fertile MORB source with greater than 0.3 wt.% Fe_2O_3.

Published by Elsevier B.V.

1. Introduction

Oxygen fugacity (fO_2) is an intensive thermodynamic property that fundamentally regulates igneous processes by governing the likely speciation of multi-valent elements such as Fe, S, and V, thereby controlling their availability to participate in chemical reactions. Upper mantle processes critically affected by fO_2 include, but are not limited to, magmatic phase relations during melting and crystallization, trace element partitioning, the depth of melt initiation, and volcanic degassing (e.g., Ballhaus, 1993; Canil, 1999; Eggler and Baker, 1982; Eugster, 1959; Holloway and Blank, 1994). In multi-component systems, the relationship between iron oxidation state and oxygen fugacity is not always straightforward, and there is seldom consensus on which variable is dependent and which is independent (Canil et al., 1994; Frost, 1991; Herd, 2008; McCammon, 2005). The oxidation state of iron in basaltic glasses, on the other hand, directly relates to the fO_2 of the solid mantle from which it derives because melts are free of crystal chemical constraints (Carmichael, 1991; Herd, 2008; Kress and Carmichael, 1991).

The $Fe^{3+}/\sum Fe$ ratio $[Fe^{3+}/(Fe^{2+} + Fe^{3+})]$ of basaltic glass can be quantified by comparing the X-ray absorption spectra of unknown basaltic glasses to the spectra of basaltic glasses of similar composition (Berry et al., 2003; Cottrell et al., 2009; Wilke et al., 2005). Synchrotron-facilitated micro X-ray Absorption Near Edge Structure (μXANES or XANES) spectroscopy affords non-destructive micro-analytical determination of multi-valent element speciation at the same spatial scales as other micro-analytical techniques, allowing element oxidation state to be directly related to other geochemical proxies in microscopic glass samples.

The premise of this study is to re-assess the oxidation state of Fe in mid-ocean ridge basalts using μ-XANES, a microbeam technique that samples glass only, and to explore global relationships between $Fe^{3+}/\sum Fe$ ratios and major element chemistry, magmatic water concentration, and trace elements. We report and compare new measurements of $Fe^{3+}/\sum Fe$ ratios of global mid-ocean ridge basalt glasses (hereafter referred to as 'MORB') using several methods, and show that MORBs are uniformly more oxidized than prior studies have indicated. These results place new constraints on the fO_2s relevant for MORB magmas and the Fe^{3+} concentrations expected in mantle sources. We will examine the implications of these findings for the evolution of $Fe^{3+}/\sum Fe$ ratios in MORB magmatic systems during low-pressure crystal fractionation, for the Fe^{3+}

* Corresponding author. Tel.: + 1 202 633 1859.
  E-mail address: CottrellE@si.edu (E. Cottrell).

concentration of the MORB mantle, and for the mechanisms controlling fO_2 of the MORB mantle during melting beneath mid-ocean ridges.

2. Methods

2.1. Samples and preparation

Natural samples analyzed in this study include pillow-rim basaltic glasses from a global distribution of mid-ocean ridges (Supplemental Fig. 1) with a particular emphasis on choosing glasses common to the studies of Christie et al. (1986) and/or Bezos and Humler (2005) (hereafter referred to as CCL86 and BH05, respectively). Two experiments were carried out to create glasses for wet chemical and XANES analysis for the present study at QFM-5.0 and QFM-1.0, using the AII basalt starting material and experimental procedures detailed in Cottrell et al. (2009). We also prepared all of the experimental glasses (n = 6) from the original study of Kress and Carmichael (1991) provided by V. Kress.

For microbeam analysis, natural and experimental glass chips were hand-picked from the Smithsonian Sea Floor Glass Collection, from experimental run products, or from pre-picked splits sent from donors or other repositories. Samples were mounted in epoxy, double-side polished to a nominal thickness of 100 μm, and photographed in reflected, plane-polarized, and cross-polarized light to ensure a crystal-free path for infrared and X-ray microbeams. In addition to glass wafers, chips and powders were prepared for $Fe^{3+}/\sum Fe$ determinations by wet chemistry (micro-colorimetry) and Mössbauer spectroscopy. In some cases, original glass powders from the micro-colorimetric study of CCL86 were available for reanalysis.

2.2. Analytical methods

2.2.1. μ-XANES

Glass wafers were analyzed by collecting three Fe K-edge XANES spectra per sample, each on an independent 9×5 μm spot, at station X26A (bending magnet) at the National Synchrotron Light Source (NSLS), Brookhaven National Laboratory (BNL). Spectral collection and fitting details are given in full in Cottrell et al. (2009), and an overview is provided in the electronic supplement. The $Fe^{3+}/\sum Fe$ ratios of MORB glasses were quantified by referencing the drift-corrected centroid (the area-weighted energy of the pre-edge $1s \rightarrow 3d$ multiplet) to a calibration curve constructed from experimental basaltic glasses. The 13 calibration glasses were equilibrated at 1 atm over a range of oxygen fugacities, from 2 log units below to 4.5 log units above the Quartz–Fayalite–Magnetite (QFM) buffer, and span a range of basalt compositions appropriate for MORB (average $\sum d_i X_i = 0.18 \pm 0.01$, defined in Table 2). The $Fe^{3+}/\sum Fe$ ratios of these reference glasses were determined with Mössbauer spectroscopy and range from 0.088 to 0.611. The 1 σ uncertainty in $Fe^{3+}/\sum Fe$ ratio measured by XANES on unknowns for this range of oxidation states is ± 0.0045 (Cottrell et al., 2009).

2.2.2. Electron microprobe analysis

Major element compositions of glasses new to this study were determined by electron microprobe at the Smithsonian Institution according to Melson et al. (2002). In all other cases we report the published values. The total iron concentrations, FeO*, of glasses used for wet chemical determination of $Fe^{3+}/\sum Fe$ ratio for this study were all obtained on the Smithsonian microprobe. Additional details and analyses are provided in the electronic supplements.

2.2.3. Mössbauer spectroscopy

Mössbauer spectra of two hand-picked MORB glasses were acquired and analyzed at the Geophysical Laboratory, Carnegie Institution of Washington, according to the procedures detailed in Cottrell et al. (2009) and Supplemental Fig. 3.

2.2.4. Fourier transform infrared spectroscopy

Transmittance FTIR spectra were obtained at the Smithsonian Institution or at NSLS station U10B over the 700–6000 cm^{-1} wavenumber range. We determined total water concentrations (molecular H_2O plus OH^-) from the intensity of the broad 3530 cm^{-1} absorption band, utilizing a molar absorptivity of 63 l/mol cm (Dixon et al., 1995) and a glass density of 2800 g/l. Thicknesses were determined using a piezoelectric digital micrometer and interference fringe patterns (Nichols and Wysoczanski, 2007). In all cases the absorption at this peak position was less than 0.8 above the baseline, and no systematic offset was observed between water concentrations derived from spectra collected at Smithsonian and the NSLS. Additional details are provided in the electronic supplement.

2.2.5. Microcolorimetry (wet chemistry)

The FeO content of select natural MORB and experimental glasses was determined using the micro-colorimetric procedure of CCL86, modified from Wilson (1960). Analyses were carried out blind, in collaboration with Dr. Rebecca Lange at the University of Michigan. Four USGS powdered rock standards were run in each analytical session. Analyses of these USGS standards never deviated from the certified FeO content by more than 0.16 wt.% FeO, well within the established analytical precision of ± 0.22 (1 σ, absolute). Additional details are provided in the electronic supplement.

2.2.6. LA-ICPMS

Trace element concentrations of wafered MORB glasses were determined by Laser Ablation Inductively-Coupled Plasma Mass Spectrometry (LA-ICPMS) at the Graduate School of Oceanography, University of Rhode Island. Analytical methods are modified from the techniques of Kelley et al. (2003). On average, triplicate analyses of
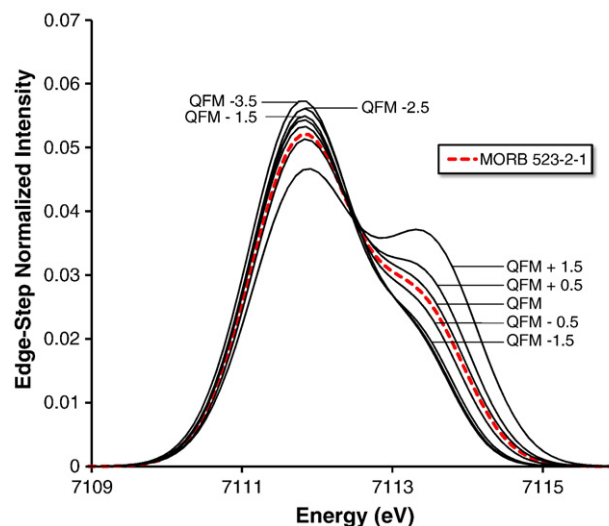

Fig. 1. Plot of energy vs. intensity for edge-step normalized, baseline-subtracted Fe K-edge XANES fluorescence spectra. Reference glasses were equilibrated in 1/2 log unit steps (Δ0.02–0.03 in $Fe^{3+}/\sum Fe$). Baseline-subtracted, drift-corrected pre-edge peaks for calibration glasses are shown at 1 log unit steps (plus a glass at QFM = 0) in fO_2 (solid lines) for clarity. All full raw spectra for these glasses, spanning the energy range from 7100 to 7200 eV and corrected only for instrumental energy drift, are presented in Cottrell et al. (2009). The area-weighted average energy of the pre-edge peaks is defined as the centroid, which shifts to higher energies as a function of iron oxidation state. As the percentage of Fe^{3+} increases above 10% of total Fe, the centroid shifts clearly to higher energies and the $Fe^{3+}/\sum Fe$ ratio is easily quantified. It is difficult to use the pre-edge centroid to quantify the $Fe^{3+}/\sum Fe$ ratio when the ferric iron contribution falls below 9% of the total iron because octahedrally coordinated Fe^{2+} has an electronic transition to a 3d-like electronic level that contributes to the spectra of reduced glasses near 7113 eV (referenced to glass LW_0≡7113.3 eV). Also plotted is a typical baseline-subtracted pre-edge of a mid-ocean ridge basaltic glass (dashed line) that can clearly be seen to fall between calibration glasses equilibrated between QFM-0.5 and QFM (~14 and 16% of iron in the ferric state, respectively).

each sample agree within 3% rsd or less for all elements reported. Additional details are provided in the electronic supplement.

3. Results

3.1. Accuracy of XANES for the assessment of $Fe^{3+}/\sum Fe$ in MORB Part I: Range in $Fe^{3+}/\sum Fe$ that can be accurately and precisely quantified with XANES

The μ-XANES pre-edge centroid position can be used to determine $Fe^{3+}/\sum Fe$ ratios in basaltic glasses from ~0.09 (~QFM-2), to >0.60 (~QFM+4.5), with a precision of ± 0.0045 using the procedures of Cottrell et al. (2009). Representative baseline-subtracted pre-edge spectra for reference glasses are shown in Fig. 1. We also plot a typical baseline-subtracted spectrum of a MORB glass, which can clearly be seen to fall between basalts equilibrated at QFM and QFM-0.5 ($Fe^{3+}/\sum Fe \approx 0.16$ and 0.14, respectively).

Precise and accurate quantification of $Fe^{3+}/\sum Fe$ ratios greater than 0.60 may be achievable, but is beyond the range of our calibration. The shape of the calibration curve suggests that precise quantification of the $Fe^{3+}/\sum Fe$ ratio using the pre-edge centroid will be challenging when $Fe^{3+}/\sum Fe > 0.80$ (Cottrell et al., 2009; Wilke et al., 2005). Use of the pre-edge centroid to quantify $Fe^{3+}/\sum Fe < 0.09$ is prohibited by crystal field effects. The coordination of Fe in glasses is poorly constrained, but ranges from tetrahedral to octahedral (Mysen and Richet, 2005 and references therein). Both tetrahedrally and octahedrally coordinated Fe^{2+} have electronic transitions corresponding to 3d-like electronic levels that occur near 7113 eV, which overlap the energy range of the main contribution from Fe^{3+} (Galoisy et al., 2001; Westre et al., 1997). We observe that the centroid ceases to shift to lower energies as a function of ferric iron content below ~9% such that the centroid of a glass with 0% ferric iron is essentially indistinguishable from a glass with 8% ferric iron (Fig. 1 and Supplemental Fig. 2).

To rigorously test this observation, experiment AII_-50 was equilibrated at QFM-5 to ensure that 100% of the iron was in the ferrous state. Wet chemical analysis confirmed the absence of any ferric iron (Table 1 and Fig. 2). Relative to reference glass LW_0 (QFM=0) with a centroid of 7112.300, the centroid of AII_-50 is 7112.071 ± 0.016, the same within error as glass equilibrated at QFM-3.0 (Cottrell et al., 2009). A shoulder is clearly visible in the baseline subtracted spectra in the region overlapping electronic transitions corresponding to ferric iron (Supplemental Fig. 2). The centroid of AII_-50 would correspond to $Fe^{3+}/\sum Fe = 0.082$ if analyzed as an

Table 1
Wet-chemical results (micro-colorimetry) compared to Mössbauer/XANES results.

Sample	FeO (wt.%) wet chemistry			FeO* (wt.%)		Fe³⁺/ΣFe wet chemistry					Fe³⁺/ΣFe spectroscopy	
	This study	Christie et al. (1986)	Bezos and Humler (2005)	SI	Christie et al. (1986)	This study SI FeO*	This study and Christie et al. (1986) FeO*[a]	Christie et al. (1986)	Bezos and Humler (2005)	Predicted/ reported K and C[b] (1991)	MÖSS	XANES[h]
Experimental basalts [c]												
AII_-50	7.35			6.98		– 0.053				0.00	b.d	0.082
AII_-50R[d]	7.25			6.98		– 0.039				0.00		
Q62[e]										0.63	n.a.	0.628
Q65[e]	5.38			16.00		0.663				0.64	n.a.	0.620
Q66[e]	5.62			15.47		0.637				0.62	n.a.	0.617
Q61[e,f]										0.67 [f]	n.a.	0.647
Q51[e,f]										0.75 [f]	n.a.	0.700
Q53[e,f]										0.75 [f]	n.a.	0.709
LW_20[g]	7.42			10.68		0.306				0.30	0.30	0.303
AII_15[g]	7.47			9.33		0.200				0.26	0.25	0.247
AII_-10	8.55			9.40		0.090				0.10	n.a.	0.116
Natural basalts [h]												
JDF C6-1												0.165
JDF C6-1 (VG chip)	10.16	10.41	9.78	11.57	11.14	0.122	0.088	0.066	0.123			
JDF C6-1 (Carmichael pwd[i])	10.42	10.41	9.78	11.57	11.14	0.099	0.065	0.066	0.123			
CH33-1												0.153
CH33-1 (VG chip)	8.62	9.29	8.73	9.88	9.72	0.128	0.114	0.044	0.102			
CH33-1R[d] (VG chip)	9.13	9.29	8.73	9.88	9.72	0.076	0.060	0.044	0.102			
CH33-1_R[d]3 (VG chip)	8.79	9.29	8.73	9.88	9.72	0.110	0.095	0.044	0.102			
CH33-4_R[d]4 (VG chip)	9.00	9.29	8.73	9.88	9.72	0.089	0.074	0.044	0.102			
CH61-1												0.163
CH61-1 (Langmuir chip[i])	8.28	9.14		10.05	9.93	0.177	0.167	0.072			
CH61-1 (Carmichael pwd)	8.60	9.14		10.05	9.93	0.144	0.134	0.072			
CH5-1 (VG chip)	9.60	10.16		11.16	11.13	0.140	0.138	0.087			0.166
VG3385, 523-2-1 (VG chip)	9.50	9.28	9.12	10.37	10.05	0.084	0.055	0.077	0.093	0.16	0.143
VG8488, 2πD47-1 (VG chip)	8.59		8.30	9.43		0.089	0.093		0.124	0.17	0.159
USNM 113716 (VG chip)	8.36			9.13		0.085						0.150
JDF C2-1 (Carmichael pwd)	11.95	11.76	12.03	14.31	13.78	0.165	0.133	0.146	0.127		0.160
975-5-1 (Langmuir chip)	9.35	9.59		10.68	10.34	0.125	0.096	0.072			0.165
CH6-1 (VG chip)	8.43	9.41		10.40	10.26	0.189	0.178	0.080			0.162
CH30-1 (Langmuir chip)	10.47	10.65		11.51	11.62	0.090	0.099	0.080			0.167

[a] The $Fe^{3+}/\sum Fe$ ratio calculated from the FeO measured in this study via micro-colorimetry combined with the FeO* from Christie et al. (1986).
[b] Calculated from Kress and Carmichael (1991) equation (7) or measurements reported in that paper.
[c] Additional data plotted in Fig. 2 are from Cottrell et al. (2009).
[d] "R" = replicate analysis.
[e] Samples from Kress and Carmichael (1991). Provided by Victor Kress.
[f] These glasses fall outside of our XANES calibration range.
[g] From Cottrell et al. (2009).
[h] All XANES measurements taken on wafered glass chips.
[i] Wet chemistry performed on powder from the study of Christie et al. (1986), provided by Ian Carmichael, or on chips of glass provided by Charlie Langmuir.

unknown (Fig. 2). As the ferric iron content drops below 10% we observe that centroid values cease to decrease systematically in the calibration curves of Berry et al. (2008), Cottrell et al. (2009), Wilke et al. (2005), and calibration curves compiled from the literature shown in Cottrell et al. (2009).

The critical result is that the pre-edge centroid can only place an upper limit on the ferric iron content of samples with <8–9% of their iron in the ferric state. Caution should be exercised when centroid values fall near the lower end of the calibration range ($Fe^{3+}/\sum Fe \leq 10\%$), such as for lunar glasses and Archean melt inclusions (Berry et al., 2008).

3.2. Accuracy of XANES for the assessment of $Fe^{3+}/\sum Fe$ in MORB Part II: Direct comparison with wet chemistry

The $Fe^{3+}/\sum Fe$ ratios of the calibration glasses used in this study were independently determined by Mössbauer spectroscopy and in Fig. 2 those determinations are compared to the $Fe^{3+}/\sum Fe$ ratios

Fig. 2. Comparison of $Fe^{3+}/\sum Fe$ ratios in glasses determined by Mössbauer-based XANES relative to ratios determined by wet chemical techniques or algorithms based on wet chemical data. The solid line shows 1:1 correspondence. (a) The open circles are calibration glasses from Cottrell et al. (2009), which provide the XANES calibration. Their Mössbauer-derived $Fe^{3+}/\sum Fe$ ratios are plotted against the $Fe^{3+}/\sum Fe$ ratios predicted by the Kress and Carmichael (1991) algorithm, which is based on micro-colorimetric wet chemical data, for the set of $\sum d_i X_i$–P–T–fO_2 under which they were equilibrated. The dashed line shows a linear regression through these data ($y = 0.9782$ x $- 0.008$, $R^2 = 0.99$). The solid diamonds are experimental basaltic glasses analyzed directly by both XANES and micro-colorimetry. Two glasses (AII_-50 and AII_-10) were created for this study. Of the other experimental glasses, two are calibration glasses from Cottrell et al. (2009) and six are from the study of Kress and Carmichael (1991) and were provided by V. Kress. Two of the Kress and Carmichael glasses have analyses via XANES plotted against micro-colorimetry performed in this study (solid black diamonds) and all six against the original micro-colorimetry results reported by Kress and Carmichael (1991) (shaded triangles). XANES results for natural basalts are plotted against micro-colorimetric analyses carried out in this study (solid black circles), the study of Christie et al. (1986) (crosses) and the direct titration wet chemical study of Bezos and Humler (2005) (shaded squares). The large shaded area represents the range of $Fe^{3+}/\sum Fe$ values that are poorly quantified by XANES. (b) Expanded view of the open boxed area of (a). Black horizontal bars compare XANES measurements to direct analysis of basalt glass powders by Mössbauer spectroscopy. Boxed cross is USNM 113716. Overlain open symbols indicate replicate analyses of the same basalt pillow (bull's-eye, CH 33; white cross, CH 61-1; white bar, JDF C6-1).

expected from the composition-dependent empirical expression that relates fO_2 to iron oxidation state determined with micro-colorimetry (Kress and Carmichael, 1991). Kress and Carmichael (1991) and CCL86 employed the same wet chemical technique applied here. The $Fe^{3+}/\sum Fe$ ratios of experimental glasses directly determined by micro-colorimetry in this study are also compared to the Mössbauer-based XANES calibration of Cottrell et al. (2009) in Fig. 2. The two determinations, by Mössbauer and by (or referenced to) wet chemistry, are strongly correlated ($R^2 = 0.99$), but the XANES calibration is systematically offset to higher Fe oxidation state by 0.01 (absolute). Potential offsets between Mössbauer and wet chemical determinations of iron oxidation state have been debated in the literature (Dingwell, 1991; Dyar et al., 1987; Lange and Carmichael, 1989; Mysen et al., 1985; Ottonello et al., 2001). The practical result for the present study is that, if we reconstruct our XANES calibration using the Kress and Carmichael (1991) algorithm, the $Fe^{3+}/\sum Fe$ ratio of unknown basalts would shift to more reduced values by 0.01 (absolute), or <10% (relative).

The majority of the experimental glasses from the XANES calibration suite were pressed into pellets for Mössbauer analysis, rendering them unsuitable for wet chemical analysis. Two experiments, equilibrated at QFM + 2 and QFM + 1.5, had enough glass remaining to perform micro-colorimetric determination of $Fe^{3+}/\sum Fe$. An additional experiment at QFM - 1 was undertaken for micro-colorimetric analysis (AII_-10, spectrum in Supplemental Fig. 2) and this experiment falls precisely on the XANES calibration curve at the expected $Fe^{3+}/\sum Fe$ ratio of 0.12. Two experiments provided by V. Kress from the original study of Kress and Carmichael (1991) were analyzed by XANES and reanalyzed by micro-colorimetry in R. Lange's lab at U. Michigan.

Glasses analyzed in this study by wet chemistry are tabulated in Table 1. The $Fe^{3+}/\sum Fe$ ratios of the five experimental basalts determined by micro-colorimetry in this study are consistent with the ratios predicted from the Kress and Carmichael (1991) algorithm, and the Mössbauer-based XANES calibration (Table 1; Fig. 2a). Micro-colorimetic and XANES results on glasses provided by V. Kress were identical within error. Given all of these tests, we are confident that micro-colorimetry and our Mössbauer-based XANES calibration return the same $Fe^{3+}/\sum Fe$ ratios on experimental glasses to within 0.01–0.02 absolute across our calibration range.

Twelve natural MORB glasses were selected for micro-colorimetric analysis in this study, ten of which are common to the studies of CCL86 and/or BH05, as indicated in Table 1. Replicate analyses were
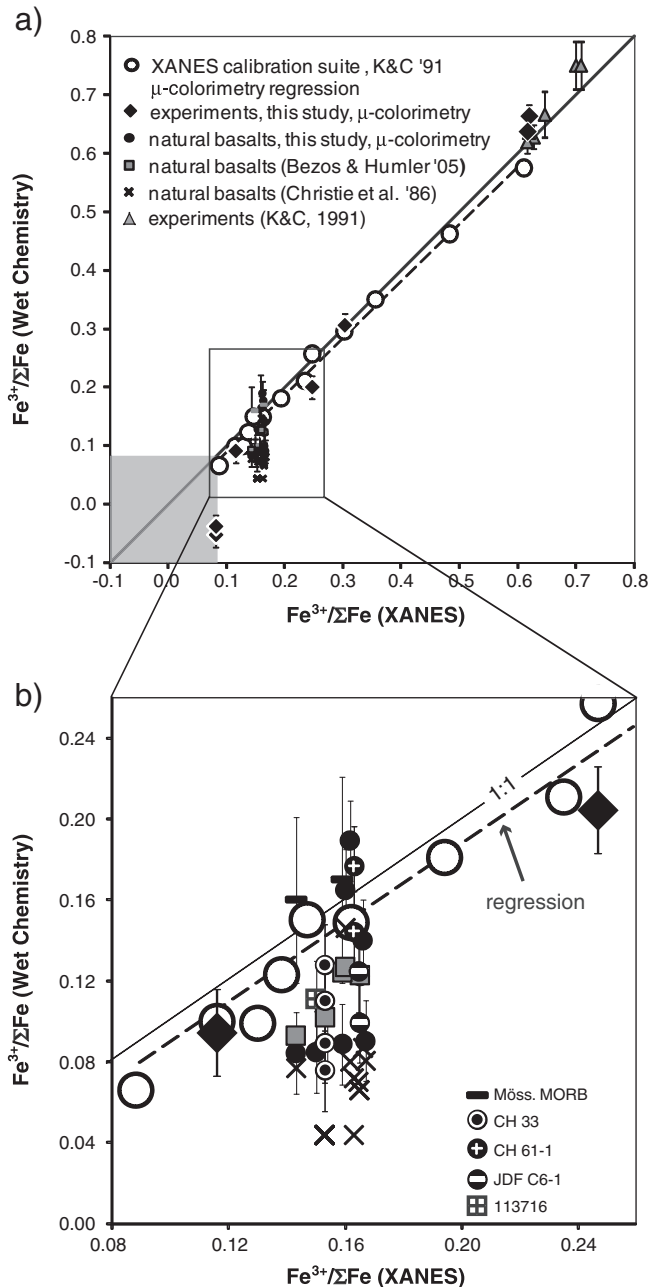
performed on three of the basalts and in some cases analyses were performed on original powders from the study of CCL86. Unlike the experiments, micro-colorimetric determination of the natural basalts fell on average to lower $Fe^{3+}/\sum Fe$ ratios relative to XANES (0.120 ± 0.035 vs. 0.159 ± 0.007), and spanned a range from more reduced values to more oxidized values (Fig. 2). Replicate analyses of sample CH 33-1 varied in $Fe^{3+}/\sum Fe$ ratio by up to 0.05 (absolute), outside of analytical error. For the samples in common with CCL86, FeO values measured in this study are systematically offset to lower FeO contents by an average of 0.3 wt.% FeO, and CCL86 do not report analyses of standards to provide a baseline for comparison. We observe no offset between the wet chemical determinations made by BH05 and micro-colorimetry in this study, despite the differences in analytical procedure. Relative to XANES determinations, however, the $Fe^{3+}/\sum Fe$ ratios measured by BH05 are systematically lower by 0.04 absolute (25%) than measured by XANES, and those measured by CCL86 are lower by 0.09 absolute on average (56%). In these calculations, we have used total iron concentrations obtained for the glass on the Smithsonian microprobe. The greatest accuracy would be achieved by using total iron obtained on the bulk sample, although using the bulk values reported for $Fe_2O_3^*$ (converted to FeO^*) by CCL86 does not nullify the discrepancy. For the samples from CCL86 analyzed in this study by micro-colorimetry, the average $Fe^{3+}/\sum Fe = 0.124$, whereas CCL86 report 0.069, and substituting the CCL86 bulk values for FeO^* lowers the average $Fe^{3+}/\sum Fe$ ratio determined in this study to only 0.107 (also see discussion by BH05).

3.3. Accuracy of XANES for the assessment of $Fe^{3+}/\sum Fe$ in MORB Part III: Factors that could lead to an offset between XANES and wet chemistry

We investigated the possibility that iron coordination changes during the slower quench rate of natural basalts might lead to shifts in the XANES spectra relative to rapidly-quenched experimental glasses. Pillow basalts quench extremely rapidly at the outer margin, at rates of >400–1000 °C/s (Xu and Zhang, 1999; Zhou et al., 2000), and quite slowly, 2–3 °C/s maximum, deep within the spherulitic-rich margin that borders the fully crystalline interior (Fig. 3). Numerous studies have shown that slower quench rates affect only the coordination geometry and not the oxidation state of iron (Dyar and Birnie, 1984; Dyar et al., 1987; Wilke et al., 2002). Basaltic pillows therefore provide a natural laboratory in which to investigate the effect of quench rate and coordination changes on the oxidation states extracted from XANES pre-edge centroids. Fig. 3 shows a doubly-polished wafer through a MORB pillow from the Carlsberg Ridge. We acquired three XANES spectra at each of three locations: within 1 mm of the pillow rim, at 8.8 mm depth where quench crystals begin to form, and at 16.3 mm depth at the boundary with the fully crystalline pillow interior. The temperature and quench rate of these three locations as a function of time vary by over three orders of magnitude, yet all three locations recorded the same centroid position, and hence Fe oxidation state, within error. We conclude that quench rate does not influence the energy of the pre-edge centroid and this cannot be the cause of the offset between XANES and wet chemistry.
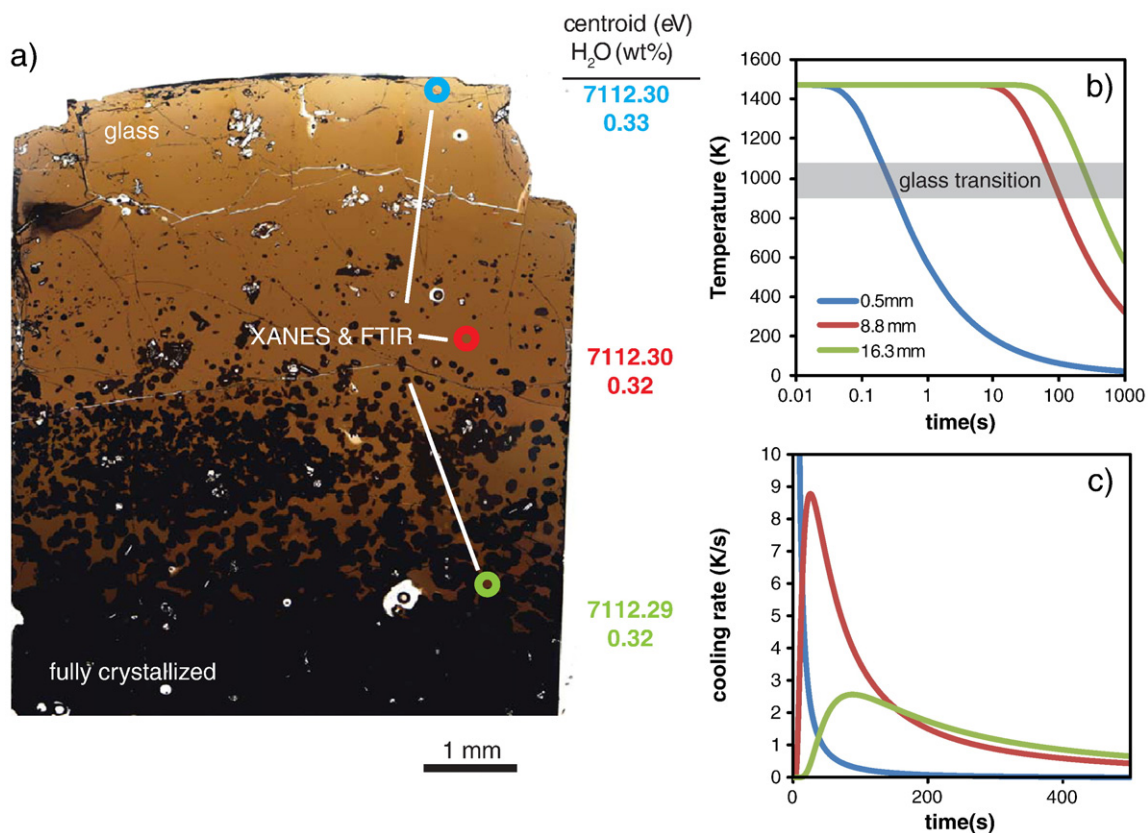

Fig. 3. Analytical and model profiles through the glassy rim of a MORB pillow. (a) Transmitted light image of a double-side polished wafer of a MORB pillow (VG 5291, NMNH catalog number 115296-3), from the crystalline interior through a spherulite-rich zone and into the glassy outer margin that was in contact with seawater. The wafer is 111 μm thick. The locations of XANES and FTIR analyses are indicated. The centroid energy positions and the $Fe^{3+}/\sum Fe$ ratios calculated from them, remain constant at all depths analyzed within the pillow, even while cooling rates vary by orders of magnitude. No variations in the total water content of the glass are observed. (b) Temperature modeled as a function of time (Carslaw and Jaeger, 1959) at the depths of the three analysis locations, with t = 0 corresponding to the time of pillow emplacement and thermal diffusivity (K) equal to 0.5 mm/s² (Hofmeister et al., 2009). The glassy rim cools to the glass transition in only a tenth of a second, whereas the spherulitic material takes minutes to reach the same temperature. Using K = 0.7 mm/s² (Bagdassarov and Dingwell, 1994) does not change the conclusions. (c) Cooling rate as a function of time for each of the three analysis points. The cooling rate at the pillow margin is >2000 K/s in the first tenth of a second following emplacement. The analysis point at 8.8 mm depth reaches a maximum cooling rate of about 9 K/s after 26 s. The deepest regions of glass never cool faster than about 2.5 K/s.
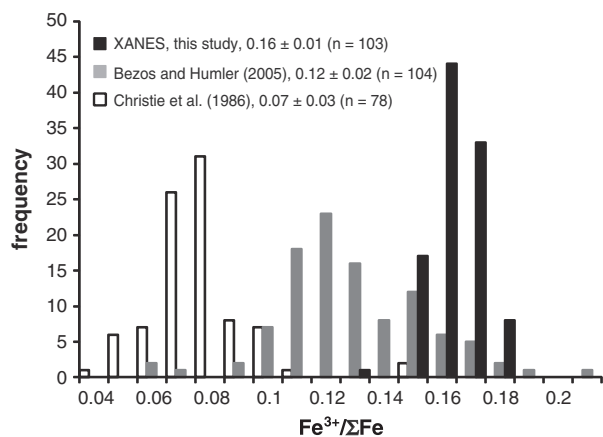
Fig. 4. Histogram showing the distribution of $Fe^{3+}/\sum Fe$ ratios of MORB glasses measured in each of three independent studies. The black bars show the XANES results of this study, grey bars indicate the wet chemical (direct titration) determinations of Bezos and Humler (2005), and the white bars indicate the wet chemical (micro-colorimetry) determinations of Christie et al. (1986). Average $Fe^{3+}/\sum Fe$ ratios for MORB glasses reported by each study are provided in the legend.

As a second check on the application of our experimentally-based calibration to natural samples, we chose two natural MORB that were particularly aphyric, and meticulously hand-picked tiny, optically transparent shards of the glass for direct Mössbauer analysis (Supplemental Fig. 3). The $Fe^{3+}/\sum Fe$ ratio obtained in this fashion was the same within error as that obtained using XANES (Fig. 2), strengthening the case that no bias should exist between spectra collected on the calibration glasses and natural samples.

There is an additional key factor that could lead to the offset between XANES and wet chemistry observed for natural samples, but not experiments. XANES inherently measures something different than wet chemistry because with XANES one has total certainty that only glass is being analyzed. Even with careful hand-picking, clusters of spherulitic or micro-phenocryst material are ubiquitous within MORB pillow glass. The presence of micro-phenocrysts, even at the very edge of the pillow, is particularly obvious when each sample is wafered to a nominal thickness of 100 µm (Fig. 3 and Supplemental Fig. 4) as was done for this study. While the dissolution of relatively Fe-free minerals like plagioclase should only have the minor effect of diluting the solution (and no effect if total iron is obtained on the bulk sample), dissolution of olivine could radically lower the $Fe^{3+}/\sum Fe$ ratio determined by wet chemistry. Four replicate analyses of sample CH 33-1, which deviate in FeO outside of analytical uncertainty, can be modeled by the addition of olivine to the wet chemical dissolutions (Supplemental Fig. 4). We show that our wet chemical analyses of CH 33-1 include 3–12 vol.% olivine, and the analysis from CCL86 must include 15 vol.% olivine (Fo_{86}). We conclude that olivine dissolution is nearly unavoidable when performing wet chemistry on MORB glasses, and that this is the primary reason for the offset between XANES and wet chemistry in natural samples.

A second major source of uncertainty in wet chemical determinations of $Fe^{3+}/\sum Fe$ derives from the need to measure both Fe^{2+} and total Fe. For example, we measured $FeO^* = 10.68$ wt.% by microprobe for MORB glass 975-5-1. The FeO^* determined for the bulk sample from CCL86 using direct current plasma (DCP) mass spectrometry is 10.34 wt.%. These values are within 3% of one another and are certainly equivalent in terms of both the accuracy and precision of the microprobe and DCP. Sample 975-5-1 was determined to have FeO = 9.75 wt.% by micro-colorimetry in this study, which translates to $Fe^{3+}/\sum Fe = 0.125$ using the Smithsonian probe value and 0.096 for the CCL86 DCP value. Small errors and biases in the measurement of total iron can therefore propagate into large uncertainty in the assessment of mantle oxidation state using wet chemical determina-

tions, whereas XANES allows direct determination of $Fe^{3+}/\sum Fe$ ratio with a single measurement.

Finally, we cannot rule out the possibility that some other redox couple absent in our experiments (e.g. S) affects the wet-chemical determinations of natural basalts, but not experimentally created ones.

3.4. $Fe^{3+}/\sum Fe$ ratio of MORB and its behavior during low-pressure fractionation

Our results show that the average $Fe^{3+}/\sum Fe$ ratio of MORB glass, as determined by µXANES measurements on 103 samples from six major spreading centers, is 0.16 ± 0.01. This average is 25% higher than that proposed by BH05 and 56% higher than that of CCL86 (Fig. 4).

As crystal fractionation proceeds and magmatic MgO decreases, we observe an increase in the $Fe^{3+}/\sum Fe$ ratio consistent with the incompatibility of Fe^{3+} during olivine fractionation ($D_{Fe_2O_3} = 0$). The effect is subtle because, even after 14% olivine fractionation (e.g., decrease in MgO from 10 to 6 wt.%), the $Fe^{3+}/\sum Fe$ ratio only increases by 0.025. The CHEPR suite from the East Pacific rise provides a wide enough range in MgO to test the global relationship on a regional scale. The trend of this regional suite is also consistent with olivine $\pm$ plagioclase $\pm$ clinopyroxene fractionation and with the trend of the global array on Fig. 5a. $Fe^{3+}/\sum Fe$ ratios also increase with moderately incompatible minor and trace element concentrations, consistent with low pressure fractional crystallization (Fig. 5b–c). Both CCL86 and BH05 observed broad increases in the $Fe^{3+}/\sum Fe$ ratio with decreasing MgO on global scales, but these were not consistent with olivine fractionation at either global or local scales. We attribute our observations to the increased precision and accuracy afforded by XANES and the certainty that XANES measures only glass.

4. Discussion

4.1. The relationship of MORB $Fe^{3+}/\sum Fe$ ratios to mantle fO_2

Having established a relationship between fractionation and $Fe^{3+}/\sum Fe$, it becomes possible to make inferences about the fO_2 of the MORB source. Kress and Carmichael (1991) provide regression coefficients for the empirical expression of Sack et al. (1980), relating the $Fe^{3+}/\sum Fe$ ratio of basalt to fO_2 at a specified temperature and for a specific composition. In order to apply these regression coefficients, the technique used to measure $Fe^{3+}/\sum Fe$ must be unbiased relative to the micro-colorimetric technique employed by Kress and Carmichael to determine $Fe^{3+}/\sum Fe$ ratios of their experiments ($n = 46$). It is unknown, for example, whether the direct titration procedure of BH05 would return the same $Fe^{3+}/\sum Fe$ ratios as micro-colorimetry if applied to the experiments of Kress and Carmichael. Moreover, in this study we have shown that micro-colorimetry may not apply equally to experimental and natural samples, suggesting that fO_2 calculated with the Kress and Carmichael algorithm from micro-colorimetry data on natural glasses may not be accurate. In the present case, we have determined that our Mössbauer-based XANES calibration is only slightly offset (0.01 absolute difference in $Fe^{3+}/\sum Fe$ ratios measured on unknowns) from the micro-colorimetric technique, and we therefore apply the Kress and Carmichael algorithm to our XANES data with reasonable confidence.

Referenced to 1200 °C and 1 atm, the average MORB from this study reflects an fO_2 of 0.10 ± 0.18 log units above the QFM buffer. At fixed oxygen content, the equilibrium fO_2 of a decompressing silicate melt roughly parallels the QFM buffer (Kress and Carmichael, 1991; O'Neill et al., 2006), such that the $Fe^{3+}/\sum Fe$ ratio of MORB provides an accurate approximation for the fO_2 of the MORB source. Selecting the most primitive glasses, for which we can reasonably assume that olivine is the only crystallizing phase (glasses with >8.5 wt.% MgO), we reconstruct primary mantle melts by incrementally adding equilibrium olivine ($D^{olv}_{Fe^{3+}} = 0$) until the melts reach equilibrium
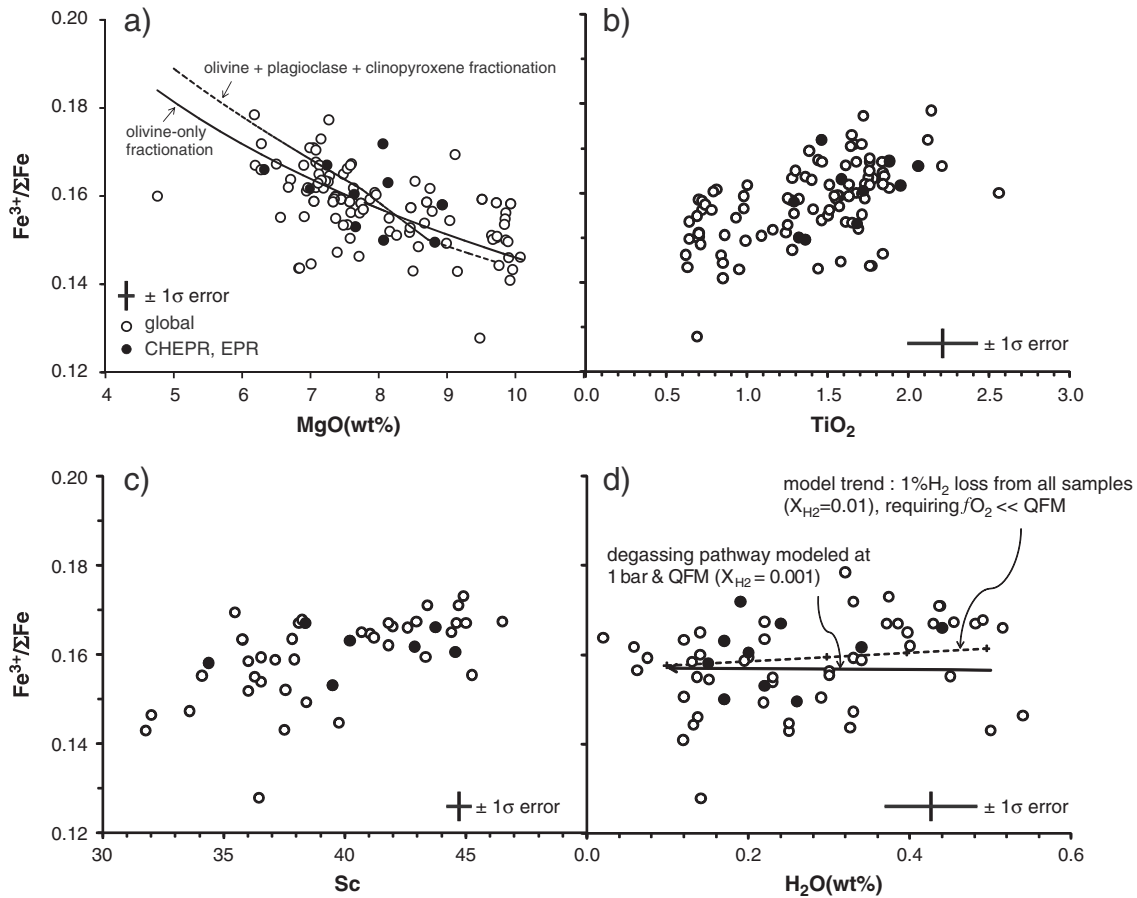
Fig. 5. (a) Plot of $Fe^{3+}/\sum Fe$ ratios in MORB as a function of MgO concentration for all samples (white circles) and those from the CHEPR cruise, 8–14°N on the East Pacific rise (black circles). The $Fe^{3+}/\sum Fe$ ratio is modeled to increase from ~0.15 to ~0.18 as MgO falls from ~10 to ~5 wt.% due to the exclusion of Fe^{3+} during closed system olivine-only (solid line) or olivine $\pm$ plagioclase $\pm$ clinopyroxene fractionation (dashed line, liquid line of descent modeled using Petrolog3 (Danyushevsky and Plechov, in press), using the mineral-melt model of Langmuir et al. (1992) and Fe^{3+} mineral/melt partition coefficients $D_{olv} = 0$, $D_{plg} = 0$, $D_{cpx} = 0.45$ (Mallmann and O'Neill, 2009)). Also shown are plots of $Fe^{3+}/\sum Fe$ ratios in MORB as a function of (b) TiO_2 and (c) Sc concentrations, with symbols as in (a). (d) Plot of $Fe^{3+}/\sum Fe$ ratios in MORBs as a function of total H_2O concentration determined by FTIR on the same glass wafers. The solid black path shows the predicted effect of H_2 loss at 1 bar and QFM during degassing from a single MORB magma, assuming an initial melt H_2O concentration of 0.5 wt.%, an initial $Fe^{3+}/\sum Fe$ ratio of 0.157, and XH_2 (fluid) = 0.001 (see discussion in text). The dashed curve shows the predicted trend if a suite of MORB magmas with initially uniform $Fe^{3+}/\sum Fe$ ratios of 0.157, but variable water concentrations, were to lose 1% of their dissolved H has H_2 gas. Such a high mole fraction of H_2 would require conditions significantly more reducing than QFM, so this curve represents an extreme upper limit (at QFM the trend would have a slope near zero and overlap the modeled degassing pathway).

with mantle olivine at Fo_{90} (Supplemental Table 2). The $Fe^{3+}/\sum Fe$ ratios of regionally averaged primary melts average 0.14 ± 0.01, or $\Delta QFM = -0.19 \pm 0.16$ at 1 atm and 1200 °C. The primary melts can also be referenced to mantle source conditions at the pressure and temperature of last equilibration using the thermobarometer of Lee et al. (2009). At average pressures of just over 1 GPa and average temperatures just above 1300 °C, the fO_2 of the MORB source is 0.07 ± 0.14 log units above QFM (Fig. 6).

The V/Sc ratio has also been developed as a proxy for oxygen fugacity, based on the observation that vanadium oxidation state, and therefore the crystal/melt partition coefficients for V, depends on fO_2 under the range of conditions expected for Earth's interior (Canil, 1997). Variations in source fO_2 may therefore be discernable using the V/Sc proxy because subsequent processes, such as crystallization, degassing, and mixing, are modeled to have only moderate effects on the V/Sc ratios of MORB magmas after they leave the mantle source (Lee et al., 2005). The V/Sc ratio of MORB in this study ranges from ~5 to 12, mirroring the global range represented in PetDB (Lehnert et al., 2000). Lee et al. (2005) modeled the expected V/Sc ratio for 10% melting of a peridotitic MORB source, such that a V/Sc ratio near 8 approximately corresponds to the QFM buffer. The V/Sc ratios of MORB from this study (>8 wt.% MgO) are consistent with the global compilation of Lee et al. (2005), and $Fe^{3+}/\sum Fe$ ratios are positively correlated with V/Sc ratios

(Fig. 6) indicating a general fidelity between these two proxies for relatively anhydrous, low melt fraction conditions. The predicted fO_2 from the V/Sc model (QFM-1 to QFM+0.25; Fig. 6b), however, is about a half log unit more reduced on average than the fO_2 we model for primary MORB melts using $Fe^{3+}/\sum Fe$ ratios (QFM-0.25 to QFM+0.50; Fig. 6a). This discrepancy is subtle, representing a shift in $Fe^{3+}/\sum Fe$ of only 0.02 (absolute). As we discuss below, other explanations, such as modification of the $Fe^{3+}/\sum Fe$ ratio due to crystallization and degassing, do not apply to these primitive, minimally degassed samples.

4.2. Do $Fe^{3+}/\sum Fe$ ratios reflect source fO_2?

The fO_2 we calculate for the MORB source is within the high end of the range of fO_2 recorded by abyssal spinel peridotites, which spans three orders of magnitude (Ballhaus, 1993; Bryndzia and Wood, 1990), and is within the range of fO_2 inferred from whole rock wet chemical analyses of MORB pillows (Carmichael and Ghiorso, 1986). Our data, therefore, do not require an ascent or post-eruptive process to modify the $Fe^{3+}/\sum Fe$ ratio of MORB glass from the $Fe^{3+}/\sum Fe$ ratio of the primary magma. CCL86 observed glassy pillow rinds to be more reduced than pillow cores and this led them to postulate that dissociation of H_2O and subsequent H_2 loss during degassing could lead to the oxidation of pillow interiors. To investigate this possibility, we analyzed a depth

profile through a pillow, from the natural surface in contact with seawater to 16.3 mm depth in the pillow, acquiring both XANES and FTIR analyses at the same points. Neither the dissolved H_2O concentration nor the oxidation state of iron in the glass changes as a function of distance from the pillow rim (Fig. 3). The homogeneity of the pillow glass on the scale of centimeters argues against a redox front passing through the cooling melt/glass, and the constancy of the dissolved H_2O concentration argues against the loss and outward diffusion of hydrogen as the glass cools.

The potential for the dissociation of H_2O, or degassing in general, to drive oxidation in terrestrial magmatic systems is often overstated. One can write a reaction whereby a melt that precipitates magnetite

a)

b)

c)

in the presence of molecular water becomes reduced by the outward migration of H_2 gas, leaving an oxidized, magnetite-rich whole rock behind (Holloway, 2004):

$$3Fe^{2+}O_{(melt)} + H_2O_{(melt)} = H_{2(fluid)} + Fe^{2+}O \cdot Fe_2^{3+}O_{3(magnetite)} \quad (1)$$
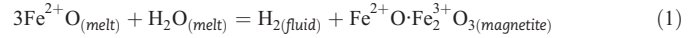
The system will be oxidized by this reaction if H_2 gas escapes the system completely. While striking examples of this phenomena have been shown for cases of low-temperature disequilibria (Castro et al., 2009), the occurrence of reaction (1) must be limited to low pressures in the presence of a strong redox gradient (e.g., lavas at the surface, Sato and Wright, 1966) because it requires the preferential migration of H_2. The MORB glasses presented here erupted under hydrostatic pressure that was greater than the pressure of H_2O saturation (Table 2), greatly limiting the possibility that degassing has driven oxidation by this process. Moreover, H speciation depends on fO_2. The H_2/H_2O ratio in the equilibrium fluid phase would be extremely low at the fO_2s relevant for MORB. For example, at 12 kb $X_{H2} < 0.0001$ in a fluid at QFM and is $<<0.001$ even at 1 bar, limiting H_2O dissociation to 0.01–0.1% (Frost and Ballhaus, 1998). Furthermore, this process is self-limiting because increasing fO_2 will drive X_{H2} in the fluid progressively downwards. Even if H_2 comprised 1% of a degassing H_2–H_2O phase, dissociation of the 0.1–0.2 wt.% H_2O in MORB would result in H_2 losses much less than 0.001 wt.%, which is insufficient to explain the dichotomy between pillow cores and rims observed by CCL86 (note: not observed in this study). Finally, as elegantly described by Carmichael (1991), the potential for H_2 loss to oxidize mantle-derived basaltic magmas must be very low, because nearly all the water in MORB is speciated as hydroxyl groups (OH⁻; Dixon et al., 1995; Stolper, 1982). Molecular water is therefore largely unavailable to participate in reaction (1).

Kelley and Cottrell (2009) observed that the $Fe^{3+}/\sum Fe$ ratios of basalts increases with dissolved H_2O concentration, but were careful to note that H_2O was unlikely to be the agent of oxidation in these magmas. Rather, the H_2O content of magmas serves as a proxy for the proximity of magmatism to subduction zones, and traces the influence of slab-derived mass fluxes on the mantle sources of subduction-related magmas. The absence of a global correlation between dissolved H_2O concentration and $Fe^{3+}/\sum Fe$ among MORB (Fig. 5d) is consistent with the thesis of Kelley and Cottrell (2009) that proximity to subduction, and not H_2O itself, leads to oxidation of the mantle source.

We also rule out the possibility that CO_2 outgassing can oxidize magmas (e.g., Mathez, 1984). At these fO_2s, carbon predominantly speciates as carbonate (CO_3^{2-}) when dissolved in basaltic melts and as carbon dioxide (CO_2) when partitioned into the vapor (Dixon et al.,
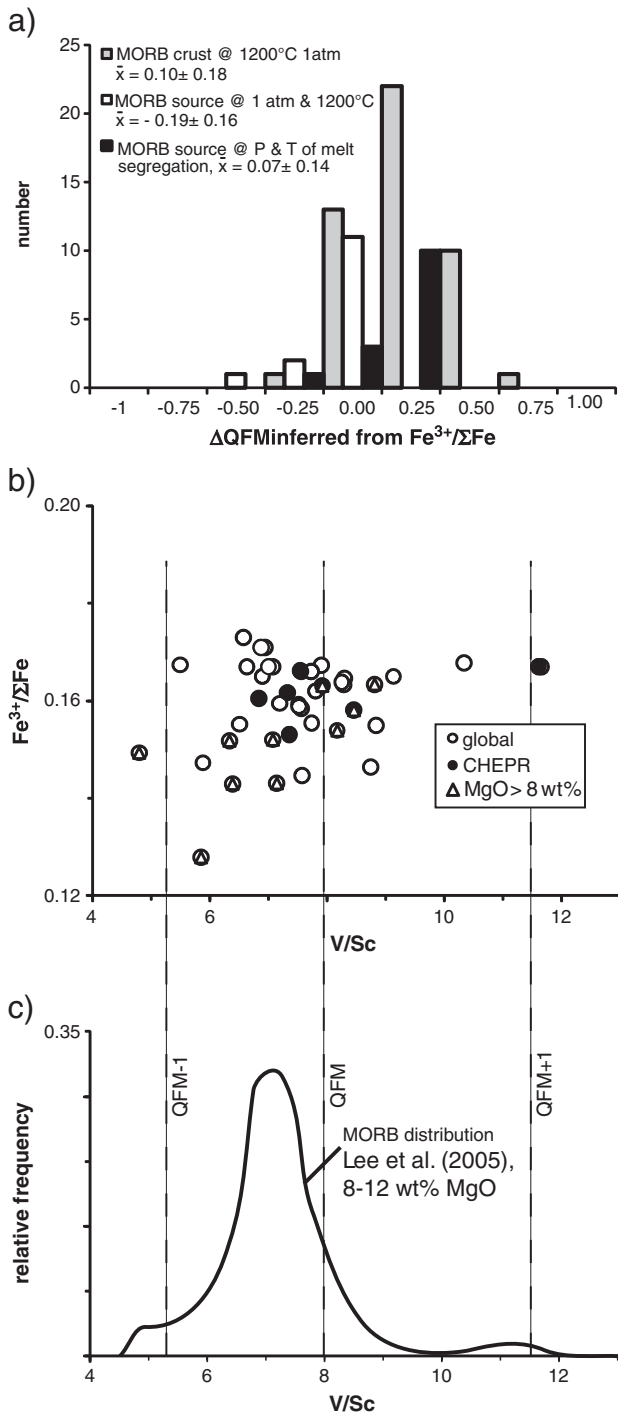
Fig. 6. (a) Histogram showing the distribution of modeled oxygen fugacities relative to the QFM buffer (Kress and Carmichael, 1991). Samples from the same region/segment/ dredge have been averaged. Grey bars relate the measured $Fe^{3+}/\sum Fe$ ratios and compositions of MORB glasses at 1200 °C and 1 atm to oxygen fugacity. White bars relate modeled primary melt compositions (samples with measured MgO concentrations higher than 8.5 wt.% that are assumed to have only olivine on the liquidus, see text for details) to fO_2 at 1 atm and 1200 °C. The addition of olivine shifts the primary melt fO_2 downward by ~0.25 log units relative to the raw data. Black bars relate those same modeled primary melts to fO_2 at the pressure and temperature of the accumulated aggregate melt, according to the thermobarometer of Lee et al. (2009), which shifts fO_2 to more oxidized values by about 0.25 log units because the average pressure of equilibration is estimated to be about 1 GPa. We estimate the fO_2 of the MORB mantle to be near the QFM buffer. (b) The $Fe^{3+}/\sum Fe$ ratios of MORB glasses plotted as a function of the vanadium to scandium ratio (V/Sc) measured on the same glass chips using LA-ICPMS. Symbols are as in Fig. 5, and samples with >8 wt.% MgO are indicated with a triangle. (c) The oxygen fugacity of the MORB source region inferred from V/Sc ratios at 10% melt fraction. The distribution of MORB lavas with 8–12 wt.% MgO is taken from Fig. 10 of Lee et al. (2005). The range of source fO_2 inferred from V/Sc ratios on samples with >8 wt.% MgO is similar to the range inferred from the $Fe^{3+}/\sum Fe$ ratios of modeled primary melts.

Table 2
Physical and analytical data for samples in this study.

Sample name	VG #	NMNH catalog number	Latitude (°N)	Longitude (°E)	Depth (mbsl)	FeO* (wt.%)	MgO (wt.%)	Na$_2$O (wt.%)	H$_2$O[a]	Fe^{3+}/∑Fe	∑d_iX_i[b]	ΔQFM	Sc (ppm)	V (ppm)
East Pacific Rise														
T558-R1	–	–	22.83	−108.12	3129	10.73	7.37	2.41	0.14	0.160	0.19	0.17		
D12-5	7172	117328-100	22.55	−108.42	2800	9.40	8.53	2.42	0.12	0.163	0.22	0.16	36	315
CH 17-4	11182	117328-53	12.86	−103.96	2632	8.76	8.07	2.60	0.17	0.150	0.23	−0.07		
CH 19-3	1187	117328-58	12.82	−103.90	2630	9.14	8.93	2.58	0.15	0.158	0.23	0.06	34	290
CH 21-1	–	–	12.78	−103.94	2623	8.93	8.82	2.38	0.26	0.150	0.21	−0.05		
CH 30-1	–	–	12.09	−103.82	2685	11.51	7.24	2.67	0.24	0.167	0.19	0.28	38	445
CH 5-1	–	–	13.75	−104.16	2660	11.16	6.32	3.39	0.44	0.166	0.22	0.20	44	330
CH 6-1	11141	117328-19	13.65	−104.17	2710	10.42	6.99	3.02	0.34	0.162	0.22	0.14	43	314
CH 61-1	–	–	8.36	−102.89	2715	10.05	8.13	2.73	0.17	0.163	0.24	0.12	40	318
CH 84-2	–	–	9.32	−104.22	2588	10.72	7.64	2.76	0.20	0.160	0.23	0.10	45	304
CH 15-2	–	–	12.85	−103.89	2640	9.51	8.06	2.56	0.19	0.172	0.23	0.28		
CH 33-1	11303	117328-116	11.77	−103.80	2900	9.88	7.66	2.38	0.22	0.153	0.19	0.06	39	290
EN113 13D-1	–	–	−24.86	−112.45	2948	8.70	8.15	3.54	0.14	0.155	0.26	−0.05		
975 5-1	7189	117328-14	22.91	−108.07	3210	10.68	7.28	2.52		0.165	0.21	0.20	41	340
RAIT 02-D120	9483	117361-114	14.59	−104.33	2797	12.97	6.18	2.75	0.32	0.178	0.15	0.56		
RAIT 02-D122	9485	117361-116	14.70	−104.33	2850	10.18	7.54	2.63		0.166	0.19	0.27	42	316
RISE 3-D30	4451	115180-3	13.83	−104.18	1458	11.96	6.28	2.85	0.33	0.172	0.18	0.38		
Siqueiros Fracture Zone														
RAIT 02 D 12-1	9377	117361-8	8.36	−104.65	3020	8.90	8.70	2.78	0.20	0.159	0.20	0.14		
SIQ D3-1	7330	116999-1	8.40	−103.94	3618	9.10	8.78	1.97	0.06	0.157	0.21	0.07		
TW74-D7-1	5211	115076-11	8.38	−103.68	3474	7.98	9.51	2.30	0.08	0.159	0.21	0.13		
SIQ D3-3	7331	116999-2	8.40	−103.94	3618	9.06	8.75	1.96	0.06	0.162	0.22	0.15		
Galapagos Spreading Center														
K 10-34	4795	115191-32	2.66	−95.49	2370	8.54	8.99	2.35	0.22	0.149	0.20	−0.02	38	184
K 14-3	4517	115194-3	2.75	−95.24	2780	11.59	6.19	2.50	0.48	0.167	0.18	0.32	38	444
K 18-21	4550	115198-21	2.60	−95.43	3220	11.18	7.08	2.33	0.49	0.168	0.16	0.36	38	395
KK78-D17-14	4956	115197-14	2.43	−95.55	2750	9.19	9.72	2.18	0.12	0.151	0.19	0.02		
KK78-D17-4	4946	115197-4	2.43	−95.55	2750	9.19	9.90	2.12	0.14	0.146	0.19	−0.05		
KK78-D17-32	4969	115197-28	2.43	−95.55	2750	9.24	9.76	2.15	0.13	0.144	0.18	−0.07		
KK78-D17-3	4945	115197-3	2.43	−95.55	2750	9.28	9.92	2.16	0.12	0.141	0.19	−0.16		
KK78-D21-2	4523	115200-2	1.64	−94.97	2750	9.58	9.04	2.27	0.15	0.154	0.18	0.11		
Indian Ocean														
V33-7-3	6647	117350-61	−49.03	124.00	2180	8.70	6.56	3.84	0.45	0.155	0.25	−0.04	34	222
V33-8-8,7	6658	117350-72	−49.27	121.03	1930	7.72	7.39	3.21	0.33	0.147	0.25	−0.16	34	197
RSR1979-011-005	5291	115296-3	−5.36	68.62	3566	10.58	6.83	3.10	0.33	0.144	0.19	−0.11		
RSR79-D 2-44	5252	115290-	9.82	57.94	3146	7.71	9.65	1.76		0.151	0.22	−0.04		
RSR79-D3-1	5253	115291-1	9.83	57.96	3066	7.64	9.67	1.69		0.150	0.22	−0.05		
RSR79-D3-4	5254	115291-2	9.83	57.96	3066	7.78	9.72	1.68		0.159	0.22	0.10		
RSR79-D3-12	5255	115291-3	9.83	57.96	3066	7.73	9.86	1.69		0.150	0.21	−0.03		
RSR79-D3-17	5256	115291-4	9.83	57.96	3066	7.78	9.86	1.71		0.156	0.21	0.06		
RSR79-D3-27	5257	115291-5	9.83	57.96	3066	7.68	9.85	1.73		0.155	0.22	0.03		
RSR79-D3-60	5258	115291-6	9.83	57.96	3066	7.75	9.93	1.76		0.158	0.22	0.09		
RSR79-D 3-60	5259	115291-7	9.83	57.96	3066	7.63	9.73	1.73		0.151	0.22	−0.04		
SI Indian Ocean probe std.	3095	113716	−24.98	69.99	3522	9.13	7.74	2.51	0.13	0.158	0.19	0.15	36	272
ANTP111-1	5917	–	−28.86	61.93	5150	8.42	7.37	4.18		0.160	0.23	0.08		
ANTP111-3	5918	–	−28.86	61.93	5150	8.64	7.33	4.25		0.159	0.23	0.06		
CIRCE110-1	5940	–	−26.62	67.53	4990	8.65	7.54	3.77		0.154	0.23	−0.02		
ANTP111-10	6770	116966-1	−28.86	61.93	5150	8.41	7.27	4.34		0.177	0.24	0.33		
CIRCE110-14	6847	116981-5	−26.62	67.53	4990	9.07	7.08	3.95		0.162	0.22	0.13		
AII 93-5-6-12	6857	116984-2	−27.60	65.84	4850	7.52	8.26	3.74		0.151	0.24	−0.08		
CIRCE110-12B	6873	116981-12	−26.62	67.53	4990	8.53	7.45	3.81		0.159	0.24	0.05		
CIRCE110-12E	6876	116981-14	−26.62	67.53	4990	8.59	7.48	3.80		0.153	0.23	−0.02		
AII 93-5-6-20G	6878	116984-13	−27.60	65.84	4850	7.90	8.46	3.60		0.153	0.22	−0.01		
KN162 D36-5	12399	117373-234	−52.749	11.711	4017	8.25	7.35	3.87		0.159	0.25	0.03		
KN162 D36-17	12402	117373-237	−52.749	11.711	4017	8.33	7.08	3.91		0.170	0.26	0.20		
KN162 D36-27	12404	117373-239	−52.749	11.711	4017	8.57	7.19	3.91		0.162	0.25	0.05		
KN162 D49-5	12427	117373-262	−52.479	12.861	4193	7.94	7.16	4.27		0.164	0.28	0.05		
KN162 D49-16	12430	117373-265	−52.479	12.861	4193	8.15	7.11	4.19		0.163	0.27	0.04		
Juan de Fuca														
VG-2	6196	111240-1	44.67	−130.33	2220	11.84	6.71	2.62	0.02	0.164	0.18	0.26	41	340
T469-24	–	–	47.95	−129.10	2207	11.08	6.27	3.00	0.52	0.166	0.21	0.22	43	329
T464-03	–	–	48.00	−129.07	2154	9.92	7.05	2.69	0.44	0.171	0.21	0.30	43	301
T471-08	–	–	47.92	−129.11	2262	10.00	6.99	2.73	0.44	0.171	0.23	0.26	45	307
T469-22	–	–	47.95	−129.10	2197	9.90	7.13	2.71	0.43	0.167	0.24	0.19	45	312
T465-01	–	–	47.97	−129.06	2330	10.45	6.68	2.76	0.40	0.162	0.19	0.21	42	326
T471-14	–	–	47.93	−129.10	2227	10.07	7.12	2.76	0.40	0.165	0.23	0.17	44	306
T469-10	–	–	47.95	−129.10	2206	10.53	6.90	2.82	0.39	0.167	0.22	0.23	45	318
T471-23	–	–	47.93	−129.10	2227	9.63	7.15	2.97	0.37	0.173	0.25	0.25	45	295
T463-04	–	–	48.00	−129.07	2141	9.09	7.58	2.46	0.37	0.167	0.23	0.20	42	277

Table 2 (continued)

Sample name	VG #	NMNH catalog number	Latitude (°N)	Longitude (°E)	Depth (mbsl)	FeO* (wt.%)	MgO (wt.%)	Na$_2$O (wt.%)	H$_2$O[a]	Fe^{3+}/∑Fe	∑d_iX_i[b]	ΔQFM	Sc (ppm)	V (ppm)
Juan de Fuca														
JDF C2-1	7455	117354-40	44.73	−130.35	2200	14.31	4.76	3.15		0.160	0.13	0.30		
JDF C6-1	7456	117354-41	44.64	−130.37	2240	11.57	7.22	2.33	0.22	0.163	0.17	0.27	38	404
JDF D11-2	7454	117354-68	44.98	−130.33	1550	10.26	7.60	2.80	0.22	0.167	0.24	0.19	47	255
JDF D5-2	7440	117354-54	44.82	−130.29	2260	10.79	7.34	2.23	0.20	0.159	0.20	0.15	43	311
JDFD2	7432	117354-46	44.61	−130.41	2240	12.22	6.50	2.62	0.45	0.167	0.17	0.34	43	339
Mid-Atlantic Ridge														
MAPCO CH98 DR12	5494	115388-2	30.25	−41.70	4200	10.61	8.16	2.86		0.152	0.19	0.05	38	265
AII 92-29-1F	P24	113707-2	23.03	−45.03	2889	10.06	7.26	3.14		0.163	0.21	0.18	36	296
2πD47-1	8488		15.90	−46.60	3760	9.48	7.87	3.07	0.33	0.159	0.22	0.11	37	274
523-1	3384	113762	36.83	−33.25	2726	9.30	8.45	2.29		0.152	0.22	−0.03	36	228
523-2-1	3385	113763	36.83	−33.25	2743	9.84	8.50	2.64	0.50	0.143	0.20	−0.14	38	268
ALV 527 1-1	3403	113811-	36.81	−33.26	2707	9.01	9.48	2.00	0.14	0.128	0.19	−0.41	36	213
TR138 11D-1	9966	116932-7	52.01	−29.95	3800	9.93	7.37	2.82	0.23	0.155	0.21	0.05	36	321
TR138 2D-2	9277	116926-2	47.05	−27.35	2975	8.21	9.15	2.37	0.25	0.143	0.20	−0.15	32	203
TR138 9D-4	9960	–	51.56	−29.92	3710	10.06	7.01	2.88	0.25	0.145	0.22	−0.15	40	301
TK 2-10	–	–	26.27	−44.73	3950	9.25	9.27	2.62		0.169	0.15	0.41	35	297
TK 3-1	–	–	26.15	−44.85	3600	9.48	7.57	2.95		0.159	0.22	0.10	37	273
EN026 10D-3g	–	–	71.89	−1.39	2900	9.68	7.59	2.44	0.76	0.156				
TR119 6D-1	7038	116920-1	35.84	−34.18	2450	9.76	7.58	2.19	0.29	0.150	0.22	−0.06		
TR119 6D-4	7039	116920-2	35.84	−34.18	2450	10.48	7.05	2.24	0.34	0.159	0.20	0.15	38	285
EN25 2D-4	6925	–	54.76	−35.22	2075	11.25	7.48	2.10	0.14	0.165	0.17	0.29	41	371
EN25 6D-3	6979	–	57.14	−33.42	760	12.20	6.91	2.07	0.30	0.155	0.15	0.19	45	350
2πD43	8482	–	13.50	−45.00	3770	9.96	7.71	2.89	0.54	0.146	0.23	−0.13	32	280
MAPCO CH98 DR11	5490	115387-2	30.70	−41.83	3640	10.30	8.67	2.53	0.23	0.154	0.19	0.09	37	298
AII107-D20-1	7298	–	−33.72	−14.25	1489	7.47	9.96	1.65		0.143	0.20	−0.13		
AII107-D20-2	7299	–	−33.72	−14.25	1489	7.55	9.84	1.66		0.154	0.21	0.03		
AII107-D20-3	7300	–	−33.72	−14.25	1489	7.48	10.07	1.64		0.146	0.20	−0.09		
AII107-D20-6	7301	–	−33.72	−14.25	1489	7.61	9.89	1.64		0.150	0.20	−0.02		
LYN73-D7	962	113181-	70.17	15.28	1097	10.03	8.00	1.72		0.156	0.20	0.16		
LYN73-D7-001	G65	–	70.17	−15.28	1097	9.97	7.94	1.72		0.161	0.21	−0.10		
LYN73-D7-002	G66	–	70.17	−15.28	1097	10.07	7.96	1.68		0.160	0.20	0.02		
LYN73-D30-012	G76	–	70.57	−14.69	1070	9.26	8.58	1.70		0.149	0.23	0.08		
LYN73-D30-014	G78	–	70.57	−14.69	1070	9.05	8.47	1.70		0.157	0.24	0.14		
American-Antarctic ridge														
VLC5-39-10	5842	115462-5	−58.65	−16.21	3822	8.89	7.72	3.44		0.156	0.23	0.02		
VLC5-39-12	5844	115462-7	−58.65	−16.21	3822	8.93	7.77	3.42		0.157	0.23	0.04		
VLC5-39-13	5845	115462-8	−58.65	−16.21	3822	9.39	6.94	3.70		0.161	0.23	0.10		
VLC5-39-17	5846	115462-9	−58.65	−16.21	3822	9.03	6.96	3.54		0.162	0.25	0.07		
VLC5-39-20	5848	115462-11	−58.65	−16.21	3822	8.93	6.84	3.54		0.144	0.25	−0.23		
VLC5-39-28	5851	115462-13	−58.65	−16.21	3822	8.95	7.63	3.42		0.162	0.23	0.12		

Additional major element data and published data sources are available in the electronic supplement.

[a] H$_2$O data and major elements on the 10 samples from Endeavor provided by P. Michael and J. Gill (pers. comm). Major element data for T558-R1 from D. Clague (pers. comm.)

[b] ∑d_iX_i parameterizes basalt composition (sum of coefficients (d_i) multiplied by oxide mole fractions (X_i), as defined in Kress and Carmichael, 1991).

1995; Stolper and Holloway, 1988). Carbon dioxide degassing is therefore redox-neutral because the degassing reaction

$$CO_3^{2-}(melt) \rightarrow CO_{2(vapor)} + O_{(melt)}^{2-} \qquad (2)$$

does not change the charge balance in the melt. More extensive discussion of the difficulty of changing magmatic redox through C–O–H degassing can be found in Ballhaus (1993), Candela (1986), and Frost and Ballhaus (1998). Sulfur does have a demonstrable theoretical and empirical capability to reduce or oxidize magmas through SO$_2$ degassing (Anderson and Wright, 1972; Gerlach, 1993; Sakai et al., 1982). Mid-ocean ridge basalts, however, are usually sulfide saturated and rarely reach saturation with SO$_2$ vapor (Mathez, 1976) and the complexities of S degassing are thus inconsequential to normal MORB systems.

4.3. The ferric iron content of the mantle

The Fe^{3+}/∑Fe ratios of basalt glasses measured in this study can be converted to Fe$_2$O$_3$ and FeO using electron microprobe measurements of total iron (FeO*, Table 2). It would be inappropriate to use FeO* values from bulk rocks because, unlike in the case of wet

chemistry, our Fe^{3+}/∑Fe ratios are measured directly on the glass. The average Fe$_2$O$_3$ of our MORB samples is 1.67 wt.%, which decreases to 1.38 wt.% for modeled MORB primary melts. For partial melts of the mantle, there is a range of Fe^{3+} bulk partition coefficients and mantle Fe$_2$O$_3$ contents (C_o) that would satisfy this liquid concentration (Fig. 7). Based on Mössbauer analyses of mineral separates from continental xenoliths, Canil et al. (1994) inferred the Fe$_2$O$_3$ content of the primitive mantle to be 0.3 wt.%, and suggested that depleted oceanic peridotite might have <0.1 wt.%. The Fe$_2$O$_3$ contents for MORB proposed in this study (and BH05), however, are consistent with 0.2–0.3 wt.% Fe$_2$O$_3$ in the MORB mantle for a typically quoted bulk $D_{Fe_2O_3} = 0.1$. Yet, recent, experimental determinations of crystal/melt partitioning of Fe^{3+} indicate that bulk mantle/melt Ds for Fe^{3+} may be significantly higher. If we apply the experimentally determined partition coefficients of Mallmann and O'Neill (2009) to a fertile mantle mode with 55% olivine, 25% orthopyroxene, 18% clinopyroxene, and 2% spinel, we calculate a bulk $D_{Fe_2O_3} = 0.22$. With this higher bulk D, the inferred Fe$_2$O$_3$ content of the MORB mantle shifts even higher, to 0.35–0.4 wt.% Fe$_2$O$_3$ (Fig. 8). Below we consider the possibility that the construct of a single partition coefficient for Fe^{3+} may be inappropriate because Fe^{3+} cannot be treated strictly as a conserved incompatible element during melting. Regardless, a

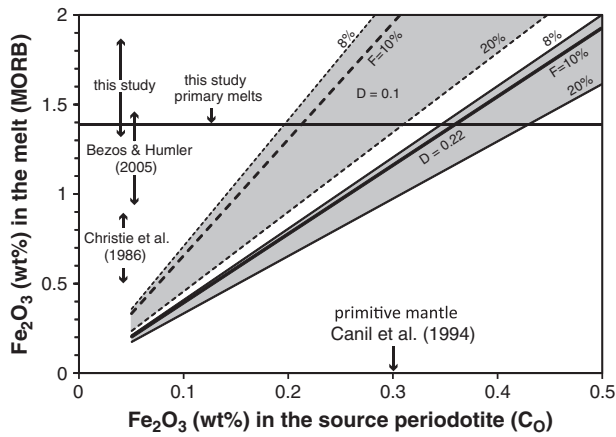**Fig. 7.** Plot of Fe_2O_3 concentrations of MORB glasses, calculated from $Fe^{3+}/\sum Fe$ ratios measured in this study using determinations of FeO^* (total iron) from microprobe, as a function of the modeled Fe_2O_3 concentration in the MORB source (peridotite) using a fractional melting model. The bold dashed line assumes a bulk ferric iron partition coefficient (D^{Fe3+}) of 0.1 (Canil et al., 1994) and 10% melt fraction (F). Lighter dashed lines delineate the envelope of melt fractions estimated for global MORBs, from F = 8–20% (Klein and Langmuir, 1987). The solid bold line assumes $D^{Fe3+} = 0.22$ (calculated from Mallmann and O'Neill, 2009; see text for details) and F = 10%, with lighter solid lines indicating the melt fraction envelope for F = 8–20%. Primary melts modeled in this study indicate that the Fe_2O_3 content of peridotite appropriate for the MORB source is between 0.2 and 0.35 wt.%, depending on the bulk partition coefficient of ferric iron.

relatively high ferric iron content for the MORB mantle is an inescapable consequence of these data.

4.4. Controls on mantle fO_2

The behavior of ferric iron and the evolution of mantle fO_2 during mantle melting are nuanced. Crystal chemistry exerts considerable control on the ferric iron contents of minerals, such that significant ferric iron can be incorporated in minerals even under reducing conditions (Frost et al., 2004; McCanta et al., 2004). Upon melting, the input of Fe^{3+} and Fe^{2+} to the melt will be governed by crystal/melt partitioning; however, the subsequent ratio of oxidized to reduced iron in the melt will reflect the prevailing system fO_2, which is itself controlled by the solid phase assemblage. For example, the ferric iron content of spinels partially defines the intrinsic fO_2 of the system and is used to record the fO_2 of the system, but is also likely to decouple from the fO_2 of the system during melting due to crystal chemical effects commensurate with Fe^{3+} extraction (Canil and O'Neill, 1996; Canil et al., 1994; Frost and McCammon, 2008; Woodland et al., 2006). Likewise, carbon present in the mantle has the potential to buffer melting through the reaction $C + O_2 \leftrightarrow CO_2$, and therefore define the fO_2, but the stability of graphite is itself controlled by fO_2 (Ballhaus, 1993; Blundy et al., 1991; Dasgupta and Hirschmann, 2010). It is therefore difficult to deconvolve the factors controlling fO_2 from those responding to it.

If Fe^{3+} behaves incompatibly during peridotite melting and mantle fO_2 is not buffered, we would expect to find a positive correlation between the $Fe_2O_3(8)$ and other incompatible elements such as $Na_2O(8)$, a canonical proxy for the extent of melting (where the (8) denotes concentrations corrected for fractional crystallization to 8 wt.% MgO, Klein and Langmuir, 1987). $Fe_2O_3(8)$, however, shows a very weak negative association, if any, with $Na_2O(8)$ consistent with the results of BH05. This observation holds on the global scale when samples from the same dredge or segment are locally averaged to prevent sampling bias ($R^2 = 0.18$) and when calculated primary melts are considered ($R^2 = 0.03$) (Fig. 8). We offer two potential explanations for this observation: either the bulk partition coefficient of ferric iron is higher than previously assumed, and potentially variable with
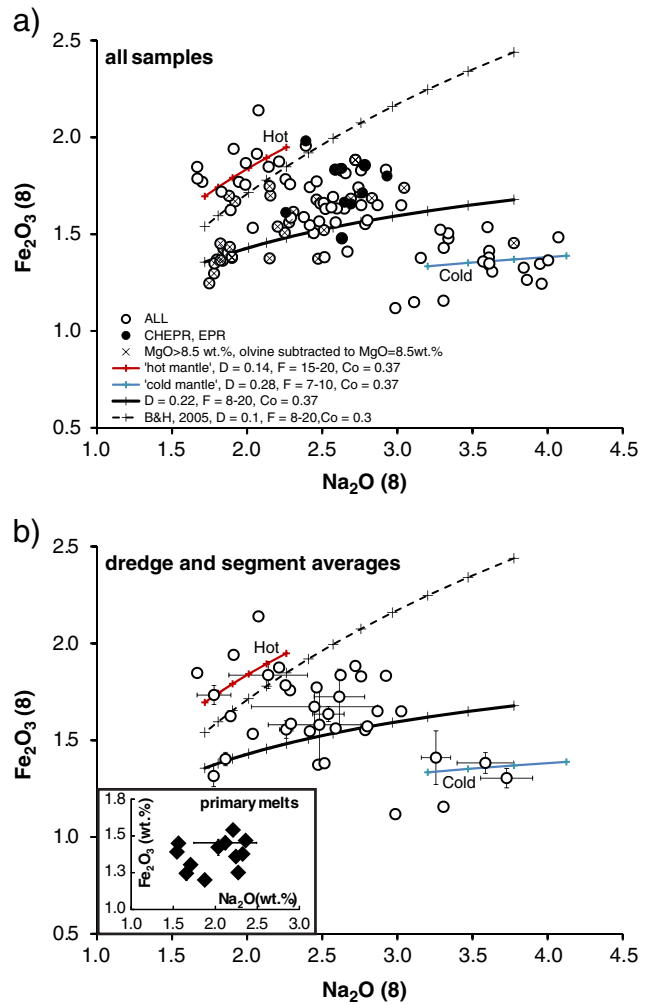

Fig. 8. Plot of $Fe_2O_3(8)$ as a function of $Na_2O(8)$. Oxide concentrations of MORB glasses were corrected for fractionation to 8 wt.% MgO ($Na_2O(8)$, Klein and Langmuir (1987); $Fe_2O_3(8) = Fe_2O_3 - 0.2074 \cdot (8 - MgO)$). Samples with measured MgO>8.5 wt.% first had olivine subtracted to 8.5 wt.% MgO and were then corrected for olivine and plagioclase fractionation to 8.0 wt.% MgO. A very weak negative correlation is present whether looking at (a) all samples or (b) regional and dredge averages. No correlation is observed among the modeled primary melts (b, inset). The expected correlations for incompatible behavior during melting are shown for an array of model assumptions about the partition coefficient of ferric iron, the extent of melting, and the initial ferric iron content of the mantle.

mantle temperature, or mantle melting is buffered at nearly constant fO_2.

The slope of the expected correlation depends on the relative difference between the bulk partition coefficient of Na (0.02–0.04, Langmuir et al., 1992) and that of Fe^{3+}. If $D_{Fe_2O_3} = 0.1$, as suggested by Canil et al. (1994) (based in part on the MORB $Fe^{3+}/\sum Fe$ ratios of CCL86), the modeled slope should be observable within the error of our measurements. The modeled slope would be close to zero, however, if $D_{Fe_2O_3} = 0.22$ (Mallmann and O'Neill, 2009). In combination with a slightly heterogeneous source ($Fe_2O_3 = 0.2–0.4$ wt.%), this would be consistent with these data (Fig. 8). If the partition coefficient of Fe^{3+} additionally varies by a factor of 1.5 to 2 over a reasonable range of mantle potential temperatures, similar to other cations (e.g. Pertermann and Hirschmann, 2003; Tuff and Gibson, 2007), then we would expect Fe^{3+} concentrations to vary as a function of mantle potential temperature, resulting in a negative trend on Fig. 8. The partition coefficient of Na is much lower than that of Fe^{3+}, and responds much more strongly to pressure than temperature (e.g. Blundy et al., 1995), such that variations in the bulk partition coefficient of Na will not affect the trends on Fig. 8. At low $Na_2O(8)$,

where we expect high melt fractions from relatively hot mantle, Fe_2O_3(8) would be elevated due to melting with a lower bulk Fe^{3+} partition coefficient. At high Na_2O(8) (low melt fractions, relatively cold mantle), Fe_2O_3(8) would be depressed due to melting with a higher bulk Fe^{3+} partition coefficient. Melting curves on Fig. 8 depict this variable partition coefficient model and match the data reasonably well. To fully test this hypothesis, we require greater knowledge of the mantle/melt partition coefficient for Fe^{3+} and more regional sample suites with well-defined liquid lines of descent that offer greater accuracy in determination of Na_2O(8) and Fe_2O_3(8).

The other possibility is that fO_2 is buffered by a reaction during melting such that incompatible ferric iron entering the melt is reduced to ferrous iron commensurate with the oxidation of some other phase. BH05 proposed that graphite could serve as the reductant; however, the proportions of ferric iron measured in both this study and the study of Bezos and Humler are far too oxidized for graphite to be stable in the MORB source (see Fig. 12 in Ballhaus (1993), for example). The carbon–carbon dioxide buffer cannot buffer melting to produce MORB.

Sulfur, by contrast, could serve as a reductant up to QFM + 1.5 (Jugo et al., 2010) via the reaction

$$S^{2-} + 8Fe^{3+} \leftrightarrow S^{6+} + 8Fe^{2+} \tag{3}$$
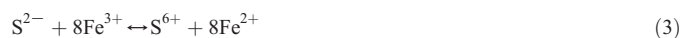
In this scenario, sulfide in the mantle would be consumed during melting while reducing ferric iron in the melt. Critically, this reaction would prevent fO_2 recorded by the $Fe^{3+}/\sum Fe$ ratios of basalts from exceeding ~QFM + 1 (see Fig. 10 in Jugo et al., 2010) even as melting preferentially extracts ferric iron from the residue. Sulfide is commonly observed in MOR basalts (Mathez, 1976) and the mantle source of MORBs is likely to contain sulfide (Herzberg, 2010; Mavrogenes and O'Neill, 1999). The sulfur concentration of the mantle (250 ppm, McDonough, 2003) exceeds that necessary to reduce all the ferric iron produced during MORB melting from F = 1–10% if $D_{Fe_2O_3} = 0.22$, half that needed if $D_{Fe_2O_3} = 0.1$, and enough in either case to reduce enough Fe^{3+} to maintain the observed $Fe^{3+}/\sum Fe$ ratios. This is because 1 mol of sulfide can reduce 8 mol of iron. Given the $Fe^{3+}/\sum Fe$ ratios of basalts measured in this study, sulfur becomes a viable candidate to buffer mantle melting, although a greater understanding of the behavior of S in the mantle source as a function of fO_2, and investigation of the speciation and concentration of S in MORB glasses, are required to fully test this hypothesis. This scenario masks, but does not lessen, the relatively high ferric iron content of >0.3 wt.% that we propose for the MORB source.

5. Conclusions

We show that μ-XANES is a highly accurate and precise technique for the determination of $Fe^{3+}/\sum Fe$ ratios in naturally quenched basaltic glass for values ranging from 0.08 to 0.61. New μ-XANES measurements of $Fe^{3+}/\sum Fe$ ratios in global MORB pillow glasses yield an average of $Fe^{3+}/\sum Fe = 0.16 \pm 0.01$, which is 25% higher than that proposed by Bezos and Humler (2005) and 56% higher than that of Christie et al. (1986). XANES determinations of $Fe^{3+}/\sum Fe$ ratios in experimental glasses are offset to more oxidized values by only 0.01 (absolute) from wet chemical determinations using micro-colorimetry. The larger interlaboratory–intertechnique offsets observed in natural samples must therefore be attributed to processes specific to the dissolution of natural lavas during wet chemical procedures.

Fe^{3+} behaves incompatibly during low-pressure fractionation but not during mantle melting. The latter may be attributed to Fe^{3+} having a higher (and potentially more variable) bulk partition coefficient than previously assumed, or melting under buffered conditions. Translation of $Fe^{3+}/\sum Fe$ ratios to solid buffers indicates that primary mantle melts form at QFM. At this oxygen fugacity, oxidation of small amounts of sulfide to sulfate would buffer the melt

and prevent magmatic $Fe^{3+}/\sum Fe$ ratios from increasing during melting. Under any model, our data indicate that the concentration of Fe_2O_3 in the fertile MORB mantle source is greater than or equal to 0.3 wt.%.

Supplementary materials related to this article can be found online at doi:10.1016/j.epsl.2011.03.014.

References

Alberto, H.V., daCunha, J.L.P., Mysen, B.O., Gil, J.M., deCampos, N.A., 1996. Analysis of Mossbauer spectra of silicate glasses using a two-dimensional Gaussian distribution of hyperfine parameters. J. Non-Cryst. Solids 194 (1–2), 48–57.

Anderson, A.T., Wright, T.L., 1972. Phenocrysts and glass inclusions and their bearing on oxidation and mixing of basaltic magmas, Kilauea Volcano, Hawaii. Am. Mineralog. 57 (1–2), 188–216.

Bagdassarov, N., Dingwell, D., 1994. Thermal properties of vesicular rhyolite. J. Volcanol. Geoth. Res. 60 (2), 179–191.

Ballhaus, C., 1993. Redox states of lithospheric and asthenospheric upper-mantle. Contrib. Mineralog. Petrol. 114 (3), 331–348.

Berry, A.J., O'Neill, H.S., Jayasuriya, K.D., Campbell, S.J., Foran, G.J., 2003. XANES calibrations for the oxidation state of iron in a silicate glass. Am. Mineralog. 88 (7), 967–977.

Berry, A.J., Danyushevsky, L.V., St, H., O'Neill, C., Newville, M., Sutton, S.R., 2008. Oxidation state of iron in komatiitic melt inclusions indicates hot Archaean mantle. Nature 455 (7215), 960–963.

Bezos, A., Humler, E., 2005. The Fe^{3+}/Sigma Fe ratios of MORB glasses and their implications for mantle melting. Geochim. Cosmochim. Acta 69 (3), 711–725.

Blundy, J., Cashman, K.V., Rust, A., Witham, F., 1991. A case for CO_2-rich arc magmas. Earth Planet. Sci. Lett. 290 (3–4), 289–301.

Blundy, J.D., Falloon, T.J., Wood, B.J., Dalton, J.A., 1995. Sodium partitioning between clinopyroxene and silicate melts. J. Geophys. Res. Solid Earth 100 (B8), 15501–15515.

Bryndzia, L.T., Wood, B.J., 1990. Oxygen thermobarometry of abyssal spinel peridotites—the redox state and C–O–H volatile composition of the Earth's sub-oceanic upper mantle. Am. J. Sci. 290 (10), 1093–1116.

Candela, P.A., 1986. The evolution of aqueous vapor from silicate melts: effect on oxygen fugacity. Geochim. Cosmochim. Acta 50, 1205–1211.

Canil, D., 1997. Vanadium partitioning and the oxidation state of Archaean komatiite magmas. Nature 389 (6653), 842–845.

Canil, D., 1999. Vanadium partitioning between orthopyroxene, spinel and silicate melt and the redox states of mantle source regions for primary magmas. Geochim. Cosmochim. Acta 63 (3–4), 557–572.

Canil, D., O'Neill, H.S.C., 1996. Distribution of ferric iron in some upper-mantle assemblages. J. Petrol. 37 (3), 609–635.

Canil, D., Oneill, H.S., Pearson, D.G., Rudnick, R.L., McDonough, W.F., Carswell, D.A., 1994. Ferric iron in peridotites and mantle oxidation-states. Earth Planet. Sci. Lett. 123 (1–4), 205–220.

Carmichael, I.S.E., 1991. The redox states of basic and silicic magmas—a reflection of their source regions. Contrib. Mineralog. Petrol. 106 (2), 129–141.

Carmichael, I.S.E., Ghiorso, M.S., 1986. Oxidation–reduction relations in basic magma—a case for homogeneous equilibria. Earth Planet. Sci. Lett. 78 (2–3), 200–210.

Carslaw, H.S., Jaeger, J.C., 1959. Conduction of Heat in Solids. Clarendon Press, Oxford.

Castro, J.M., Cottrell, E., Tuffen, H., Logan, A.V., Kelley, K.A., 2009. Spherulite crystallization induces Fe-redox redistribution in silicic melt. Chem. Geol. 268 (3–4), 272–280.

Cottrell, E., Kelley, K.A., Lanzirotti, A., Fischer, R.A., 2009. High-precision determination of iron oxidation state in silicate glasses using XANES. Chem. Geol. 268 (3–4), 167–179.

Christie, D.M., Carmichael, I.S.E., Langmuir, C.H., 1986. Oxidation-States of Midocean Ridge Basalt Glasses. Earth and Planetary Science Letters 79 (3–4), 397–411.

Danyushevsky, L. V. and P. Plechov, in press. Petrolog3: integrated software for modeling crystallization processes. Geochemistry, Geophysics, Geosystems.

Dasgupta, R., Hirschmann, M.M., 2010. The deep carbon cycle and melting in Earth's interior. Earth Planet. Sci. Lett. 298 (1–2), 1–13.

Dingwell, D.B., 1991. Redox viscometry of some Fe-bearing silicate melts. Am. Mineralog. 76 (9–10), 1560–1562.

Dixon, J.E., Stolper, E.M., Holloway, J.R., 1995. An experimental study of water and carbon dioxide solubilities in mid ocean ridge basaltic liquids. 1. Calibration and solubility models. J. Petrol. 36 (6), 1607–1631.

Dyar, M.D., Birnie, D.P., 1984. Quench media effects on iron partitioning and ordering in a lunar glass. J. Non-Cryst. Solids 67 (1–3), 397–412.

Dyar, M.D., Naney, M.T., Swanson, S.E., 1987. Effects of quench methods on Fe^{3+}/Fe^{2+} ratios—a Mossbauer and wet-chemical study. Am. Mineralog. 72 (7–8), 792–800.

Reduced volatiles in system C−O−H: implications to mantle melting, fluid formation and diamond genesis. In: Eggler, D.H., Baker, D.R. (Eds.), High Pressure Research in Geophysics. Centr Acad Publ, Tokyo.

Oxidation and reduction in metamorphism. In: Eugster, H.P. (Ed.), Researches in Geochemistry. John Wiley & Sons, New York.

Introduction to oxygen fugacity and its petrologic importance. In: Frost, B.R. (Ed.), Oxide minerals: Petrologic and magnetic significance. BookCrafters Inc, Chelsea, MI.

Frost, B.R., Ballhaus, C., 1998. Comment on "Constraints on the origin of the oxidation state of mantle overlying subduction zones: an example from Simcoe, Washington, USA". Geochim. Cosmochim. Acta 62 (2), 329–331.

Frost, D.J., McCammon, C.A., 2008. The redox state of Earth's mantle. Annu. Rev. Earth Planet. Sci. 36 (1), 389–420.

Frost, D.J., Liebske, C., Langenhorst, F., McCammon, C.A., Tronnes, R.G., Rubie, D.C., 2004. Experimental evidence for the existence of iron-rich metal in the Earth's lower mantle. Nature 428 (6981), 409–412.

Galoisy, L., Calas, G., Arrio, M.A., 2001. High-resolution XANES spectra of iron in minerals and glasses: structural information from the pre-edge region. Chem. Geol. 174 (1–3), 307–319.

Gerlach, T.M., 1993. Oxygen buffering of Kilauea Volcanic gases and the oxygen fugacity of Kilauea basalt. Geochim. Cosmochim. Acta 57 (4), 795–814.

Basalts as probes of planetary interior redox state. In: Herd, C.D.K. (Ed.), Oxygen in the Solar System. The Geochemical Society, Chantilly, VA.

Herzberg, C., 2010. Identification of source lithology in the Hawaiian and Canary Islands: implications for origins. Journal of Petrology 52(1): 113–146.

Hofmeister, A.M., Whittington, A.G., Pertermann, M., 2009. Transport properties of high albite crystals, near-endmember feldspar and pyroxene glasses, and their melts to high temperature. Contrib. Mineralog. Petrol. 158 (3), 381–400.

Holloway, J.R., 2004. Redox reactions in seafloor basalts: possible insights into silicic hydrothermal systems. Chem. Geol. 210 (1–4), 225–230.

Holloway, J.R., Blank, J.G., 1994. Application of experimental results to C−O−H species in natural melts. Volatiles Magmas 30, 187–230.

Jugo, P.J., Wilke, M., Botcharnikov, R.E., 2010. Sulfur K-edge XANES analysis of natural and synthetic basaltic glasses: implications for S speciation and S content as function of oxygen fugacity. Geochim. Cosmochim. Acta 74 (20), 5926–5938.

Kelley, K.A., Cottrell, E., 2009. Water and the oxidation state of subduction zone magmas. Science 325 (5940), 605–607.

Kelley, K.A., Cottrell, E., Brounce, M., Parks, B.H., 2010. The influence of magmatic differentiation on the oxidation state of Fe in arc magmas. Goldschmidt Conf. Abstr. A505.

Klein, E.M., Langmuir, C.H., 1987. Global correlations of ocean ridge basalt chemistry with axial depth and crustal thickness. J. Geophys. Res. Solid Earth Planets 92 (B8), 8089–8115.

Kress, V.C., Carmichael, I.S.E., 1991. The compressibility of silicate liquids containing Fe_2O_3 and the effect of composition, temperature, oxygen fugacity and pressure on their redox states. Contrib. Mineralog. Petrol. 108, 82–92.

Lange, R.A., Carmichael, I.S.E., 1989. Ferric-ferrous equilibria in Na_2O–FeO–Fe_2O_3–SiO_2 melts—effects of analytical techniques on derived partial molar volumes. Geochim. Cosmochim. Acta 53 (9), 2195–2204.

Langmuir, C., Klein, E.M., Plank, T., 1992. Petrological systematics of mid-ocean ridge basalts: constraints on melt generation beneath ocean ridges. Mantle Flow and Melt Generation at Mid-Ocean Ridges.: Geophysical Monograph 71. American Geophysical Union.

Lee, C.-T., Leeman, W.P., Canil, D., Li, Z.-X.A., 2005. Similar V/Sc systematics in MORB and arc basalts: implications for the oxygen fugacities of their mantle source regions. J. Petrol. 46 (11), 2313–2336.

Lee, C.-T., Luffi, A.P., Plank, T., Dalton, H., Leeman, W.P., 2009. Constraints on the depths and temperatures of basaltic magma generation on Earth and other terrestrial planets using new thermobarometers for mafic magmas. Earth Planet. Sci. Lett. 279.

Lehnert, K., Su, Y., Langmuir, C.H., Sarbas, B., Nohl, U., 2000. A global geochemical database structure for rocks. Geochem. Geophys. Geosyst. 1999GC000026.

Mallmann, G., O'Neill, H.S.C., 2009. The crystal/melt partitioning of v during mantle melting as a function of oxygen fugacity compared with some other elements (Al, P, Ca, Sc, Ti, Cr, Fe, Ga, Y, Zr and Nb). J. Petrol. 50 (9), 1765–1794.

Mathez, E.A., 1976. Sulfur solubility and magmatic sulfides in submarine basalt glass. J. Geophys. Res. 81, 4269–4276.

Mathez, E.A., 1984. Influence of degassing on oxidation states of basaltic magmas. Nature 310, 371–375.

Mavrogenes, J.A., O'Neill, H.S.C., 1999. The relative effects of pressure, temperature and oxygen fugacity on the solubility of sulfide in mafic magmas. Geochim. Cosmochim. Acta 63 (7–8), 1173–1180.

Mantle oxidation state and oxygen fugacity: constraints on mantle chemistry, structure and dynamics. In: McCammon, C.A. (Ed.), Earth's Deep Mantle: Structure, Composition and Evolution. American Geophysical Union, Washington, D.C.

McCanta, M.C., Dyar, M.D., Rutherford, M.J., Delaney, J.S., 2004. Iron partitioning between basaltic melts and clinopyroxene as a function of oxygen fugacity. Am. Mineralog. 89 (11–12), 1685–1693.

McDonough, W.F., 2003. Compositional model for the Earth's core. In: Carlson, R.W. (Ed.), The Mantle and Core, Treatise on Geochemistry. Elsevier-Pergamon, Oxford, pp. 547–568.

Melson, W.G., O'Hearn, T., Jarosewich, E., 2002. A data brief on the Smithsonian Abyssal Volcanic Glass Data File. Geochem. Geophys. Geosyst. 3.

Mysen, B.O., Richet, P., 2005. Silicate Glasses and Melts—Properties and Structure. Elsevier, New York.

Mysen, B.O., Carmichael, I.S.E., Virgo, D., 1985. A comparison of iron redox ratios in silicate-glasses determined by wet-chemical and Fe-57 Mossbauer resonant absorption methods. Contrib. Mineralog. Petrol. 90 (2–3), 101–106.

Nichols, A.R.L., Wysoczanski, R.J., 2007. Using micro-FTIR spectroscopy to measure volatile contents in small and unexposed inclusions hosted in olivine crystals. Chem. Geol. 242 (3–4), 371–384.

O'Neill, H.S.C., Berry, A.J., McCammon, C.C., Jayasuriya, K.D., Campbell, S.J., Foran, G., 2006. An experimental determination of the effect of pressure on the Fe^{3+}/Sigma Fe ratio of an anhydrous silicate melt to 3.0 GPa. Am. Mineralog. 91 (2–3), 404–412.

Ottonello, G., Moretti, R., Marini, L., Zuccolini, M.V., 2001. Oxidation state of iron in silicate glasses and melts: a thermochemical model. Chem. Geol. 174 (1–3), 157–179.

Pertermann, M., Hirschmann, M.M., 2003. Anhydrous partial melting experiments on MORB-like eclogite: phase relations, phase compositions and mineral-melt partitioning of major elements at 2–3 GPa. J. Petrol. 44 (12), 2173–2201.

Sack, R.O., Carmichael, I.S.E., Rivers, M., Ghiorso, M.S., 1980. Ferric-ferrous equilibria in natural silicate liquids at 1 bar. Contrib. Mineralog. Petrol. 75 (4), 369–376.

Sakai, H., Casadevall, T.J., Moore, J.G., 1982. Chemistry and isotope ratios of sulfur in basalts and volcanic gases at Kilauea Volcano, Hawaii. Geochim. Cosmochim. Acta 46 (5), 729–738.

Sato, M., Wright, T.L., 1966. Oxygen fugacities directly measured in magmatic gases. Science 153, 1103–1105.

Stolper, E., 1982. Water in silicate-glasses—an infrared spectroscopic study. Contrib. Mineralog. Petrol. 81 (1), 1–17.

Stolper, E., Holloway, J.R., 1988. Experimental-determination of the solubility of carbon-dioxide in molten basalt at low-pressure. Earth Planet. Sci. Lett. 87 (4), 397–408.

Tuff, J., Gibson, S.A., 2007. Trace-element partitioning between garnet, clinopyroxene and Fe-rich picritic melts at 3 to 7 GPa. Contrib. Mineralog. Petrol. 153 (4), 369–387.

Westre, T.A., Kennepohl, P., DeWitt, J.G., Hedman, B., Hodgson, K.O., Solomon, E.I., 1997. A multiplet analysis of Fe K-edge 1s3d pre-edge features of iron complexes. J. Am. Chem. Soc. 119, 6297–6314.

Wilke, M., Behrens, H., Burkhard, D.J.M., Rossano, S., 2002. The oxidation state of iron in silicic melt at 500 MPa water pressure. Chem. Geol. 189 (1–2), 55–67.

Wilke, M., Partzsch, G.M., Bernhardt, R., Lattard, D., 2005. Determination of the iron oxidation state in basaltic glasses using XANES at the K-edge. Chem. Geol. 220 (1–2), 143–161.

Wilson, A.D., 1960. The micro-determination of ferrous iron in silicate—minerals by a volumetric and a colorimetric method. Analyst 85 (1016), 823–827.

Woodland, A.B., Kornprobst, J., Tabit, A., 2006. Ferric iron in orogenic lherzolite massifs and controls of oxygen fugacity in the upper mantle. Lithos 89 (1–2), 222–241.

Xu, Z., Zhang, Y., 1999. Quantification of quench rates in water, air, and liquid nitrogen. Goldschmidt Conference Abstracts.

Zhou, W., Van der Voo, R., Peacor, D.R., Zhang, Y., 2000. Variable Ti-content and grain size of titanomagnetite as a function of cooling rate in very young MORB. Earth Planet. Sci. Lett. 179 (1), 9–20.